A non-intrusive reduced-order model for compressible fluid and fractured solid coupling and its application to blasting

D. Xiao[a], P. Yang[a], F. Fang[a,c,*], J. Xiang[a,c], C.C. Pain[a], I.M. Navon[b], M. Chen[c]

[a]*Applied Modelling and Computation Group, Department of Earth Science and Engineering,Imperial College London, Prince Consort Road, London, SW7 2BP, UK.URL:* `http://amcg.ese.imperial.ac.uk`
[b]*Department of Scientific Computing, Florida State University,Tallahassee, FL, 32306-4120, USA*
[c]*Wuhan University, Wuhan, 430072, China*

Abstract

This work presents the first application of a non-intrusive reduced order method to model solid interacting with compressible fluid flows to simulate crack initiation and propagation. In the high fidelity model, the coupling process is achieved by introducing a source term into the momentum equation, which represents the effects of forces of the solid on the fluid. A combined single and smeared crack model with the Mohr-Coulomb failure criterion is used to simulate crack initiation and propagation. The non-intrusive reduced order method is then applied to compressible fluid and fractured solid coupled modelling where the computational cost involved in the full high fidelity simulation is high. The non-intrusive reduced order model (NIROM) developed here is constructed through proper orthogonal decomposition (POD) and a radial basis function (RBF) multi-dimensional interpolation method.

The performance of the NIROM for solid interacting with compressible fluid flows, in the presence of fracture models, is illustrated by two complex test cases: an immersed wall in a fluid and a blasting test case. The numerical simulation results show that the NIROM is capable of capturing the details of compressible fluids and fractured solids while the CPU time is reduced by several orders of magnitude. In addition, the issue of whether or not to subtract the mean from the snapshots before applying POD is discussed in this paper. It is shown that solutions of the NIROM, without mean subtracted before constructing the POD basis, captured more details than the NIROM with mean subtracted from snapshots.

Keywords: non-intrusive, ROM, compressible fluid-solid coupling, fracturing, blasting

*Corresponding author
Email address: `f.fang@imperial.ac.uk` (F. Fang)

1. Introduction

The numerical simulation of fluid and fractured solid coupling has attracted much attention in a wide variety of research areas. This problem is of significance to many fields in engineering such as aerospace engineering, biomedical engineering, wind turbines and blasting. However, the computational cost involved in solving such complex problems is so high that this has hindered development in these areas. In order to address the issue of high computational cost, this paper proposes a non-intrusive reduced order model to solve fluid/solid coupling problems in an efficient manner.

Reduced order modelling is a technique that is capable of reducing the dimensionality of large systems, thus resulting in a considerable increase in computational efficiency. POD is the method most widely used to form reduced order models and it aims to represent a large system, with only a relatively small number of basis functions, and is optimal in the sense that they minimize the L^2 error to the training set. POD has been used successfully in various fields such as air pollution [1], ocean modelling [2], fluid mechanics [3, 4, 5], aerospace design [6], neutron photon transport [7], porous media [8], shape optimization [9] and shock problems [10]. Reduced order models (ROMs) can be derived by a combination of POD and Galerkin projection methods. However, the use of POD/Galerkin methods raises numerical instability and non-linearity inefficiency problems [11, 12, 13, 14]. Several methods have been presented to improve the numerical stability of ROMs, such as calibration [15, 16], Fourier expansion [17], regularisation [18] and Petrov−Galerkin methods [2, 19]. In order to enhance the nonlinear efficiency, various methods have been proposed, including empirical interpolation method (EIM) [20], the discrete version of EIM (DEIM) [14], quadratic expansion method [21, 22], a hybrid of DEIM and quadratic expansion (residual DEIM) method [23], a Petrov−Galerkin projection method [15], and Gauss-Newton with approximated tensors (GNAT) method [24].

Recently, there have been some works addressing reduced order modelling of fluid and solid coupling problems [25, 26, 27, 28, 29, 30]. In the work of [31], the authors presented a projection based method for contact problems. A non-negative matrix factorization scheme was used to construct positive reduced order basis functions for the contact forces. Again, those methods are intrusive, that is, they are highly dependent on the original physical system and the source code. The implementation of intrusive ROMs can be difficult, or impossible, if the source code is not available (*e.g.* commercial software) [32]. In addition, intrusive ROMs can be complex to extend to many applications such as transient problems and solid-solid contact problems.

The non-intrusive reduced order modelling technology is therefore proposed to tackle the disadvantages of intrusive ROMs, although it can have difficulty in achieving conservation. A number of non-intrusive reduced order methods have been proposed, such as a black-box stencil interpolation method [32], a POD-RBF method for unsteady fluid flows [33], a Taylor series and Smolyak sparse grid method for the Navier-Stokes equations [34], a two-level NIROM based on POD-RBF method for nonlinear parametrized PDEs [35, 36, 33], a POD-RBF for the Navier-Stokes equations [37]. NIROMs have also been applied to realistic problems such as multi-phase flow in porous media problems [38] and incompressible fluids and solids without fracturing problems [39].

This work applies the non-intrusive reduced order modelling method to compressible fluid and fractured solid problems and, more specifically, to a highly non-linear problem blasting problem. This model has been implemented under the framework of a combined finite-discrete element method based solid model (Y2D) and an unstructured mesh finite element model (Fluidity). The two models are coupled by an immersed body method, which introduces a thin shell mesh surrounding the solid surface to calculate the exchange forces between the fluid and solid. The coupling method uses three meshes for fluids, shells and solids and projects state variables on the solid mesh onto the fluid mesh via the shell mesh. This is different from the monolithic coupling approach, which treats the problem as a single mesh and the solid is treated as an internal interface [40]. In the coupling process, the state variables (velocity, pressure etc.) of the fluid dynamics on the fluid mesh (continuous mesh) are calculated and projected onto the shell mesh (continuous mesh), and these are passed onto the solid surface mesh (discontinuous mesh). The stress state is then calculated on the solid mesh. If the stress state meets a fracture failure then new discontinuous solid surfaces are generated to represent the fractures. All the discontinuous solid surfaces, including the newly generated and old discontinuous surfaces, are converted from discontinua to continua. Finally, the state variables on the solid are calculated and projected back onto the fluid mesh through the shell mesh. After the state variables arrive back on the fluid mesh, the loop starts again from 'the calculation of the state variables of the fluid'.

Non-intrusive reduced order modelling works by constructing a set of interpolation functions (hypersurfaces) to represent the underlying dynamical system in the reduced space. During the offline computational process, the solutions of the high fidelity model are recorded and a snapshot matrix for each state variable is obtained. A number of POD basis functions Φ_j, $j \in (1, \ldots, m)$ for each state variable are generated through a truncated singular value decomposition (SVD) of the snapshot matrix. A set of interpolation functions f_j ($j \in (1, \ldots, m)$ is then constructed to represent the compressible fluid and fractured solid reduced order model using the RBF-POD method. That is, the reduced order model is approximated through a linear combination of the RBFs (the Gaussian function is used here). During the online computational process, the RBFs are used to calculate the POD coefficients and the Gaussian RBF is employed here, $\alpha_j^n = f_j(\alpha^{n-1})$, where α_j^n is the j^{th} POD coefficient at current time level n and α^{n-1} is a vector of POD coefficients at previous time level $n-1$.

The mean of the snapshot matrix is normally subtracted when constructing a reduced order model. The problem of mean subtraction was discussed in [41, 42]. In their work, there was not much difference between the results with and without mean snapshot subtracted from snapshots. In this paper, whether the mean snapshot solution should be subtracted from the snapshots before constructing the POD basis functions is discussed. The performance of the NIROM constructed with and without mean snapshot subtracted from the snapshots has been assessed for two test cases: an immersed wall in a fluid and a blasting test case. It is found that the accuracy of numerical solutions can be improved when the mean of snapshots is not subtracted from snapshots before generating the POD basis functions. The high fidelity model is formed by a coupled compressible fluid and solid model and the CPU time between the high-fidelity and NIROM models are compared. The accuracy of the NIROM is also determined by comparing the high fidelity solution with the NIROM solution. The additional details

of the test cases formed by the high fidelity model can be found in the work of [43, 44].

The structure of the paper is arranged as follows: Section 2 describes briefly the compressible fluid and fractured solid problem; Section 3 derives the formulation of a non-intrusive reduced order model for compressible fluid and fractured solid problems using the POD-RBF method; Section 4 demonstrates the capability of the derived methodology through two numerical examples: an immersed wall in a fluid and a blasting test case. Finally in Section 5, the conclusions are drawn.

2. Description of compressible fluid and fractured solid problems

This section describes the governing equations, coupling methods and fracture modelling methods used in the two models: "Fluidity" (an unstructured mesh multiphase fluid model [45]) and "Y2D" (a combined finite-discrete element method based solid model [46]).

2.1. Governing equations for compressible fluids under the framework of "Fluidity"

"Fluidity" is a computational fluid dynamics open source model capable of numerically solving the 2-D and 3-D Navier-Stokes equation using the finite element discretisation method. The governing equations for compressible fluids in "Fluidity" have the following form [45, 47],

$$\frac{\partial \rho}{\partial t} + \nabla \cdot (\rho \mathbf{u}) = 0, \tag{1}$$

$$\frac{\partial}{\partial t}(\rho \mathbf{u}) + \nabla \cdot (\rho \mathbf{u} \otimes \mathbf{u} - \sigma) = \rho \mathbf{F}, \tag{2}$$

$$\frac{\partial}{\partial t}(\rho E) + \nabla \cdot (\rho E \boldsymbol{u} - \tau \boldsymbol{u} + \boldsymbol{q}) = \rho \boldsymbol{F} \boldsymbol{u}, \tag{3}$$

where ρ denotes the unknown density, $\mathbf{u}$ is the unknown velocity vector, t represents the time, σ is the stress tensor and $\sigma = \tau - pI$ (p being the unknown pressure and I the identity matrix), $\mathbf{F}$ is the volume or internal force per unit mass (*e.g.*, gravity), $\boldsymbol{q}$ denotes the heat flux, $E = e + | \boldsymbol{u} |^2 /2$ is the total specific unknown energy, and τ is the shear stress tensor in the fluid.

The density ρ is calculated by the equation of state, which is used to close the governing equation (3) [48]:

$$p = \rho(\gamma - 1)e, \tag{4}$$

where $\gamma = C_p/C_v$ is the heat capacity ratio (C_v and C_p being the specific heat at constant volume and at constant pressure respectively), and $e = C_v T$ is the internal energy per unit mass (T being the temperature).

2.2. Governing equations for solid dynamics

The solid dynamics is resolved by the combined finite-discrete element method (FEMDEM) [46, 49], which combines deformable fracturing arbitrary-shaped particle interactions modelled by the Finite Element Method (FEM) with discrete particulate

motions modelled by the Discrete Element Method (DEM). The research code Y2D is coupled with the fluid model (Fluidity). The governing equation in solid mechanics is given by:

$$\boldsymbol{F}_e + \boldsymbol{F}_v + \boldsymbol{F}_p + \boldsymbol{F}_c = m\frac{\partial \boldsymbol{u}_s}{\partial t} + \boldsymbol{F}_i, \tag{5}$$

where $\boldsymbol{F}_e$ denotes the external force, $\boldsymbol{F}_v$ is the viscous force between the solid and fluid, $\boldsymbol{F}_p$ denotes the pressure force, $\boldsymbol{F}_c$ is the contact force among multiple solids, m is the solid mass and $\boldsymbol{u}_s$ is the unknown velocity of the solid. For additional details, see [46, 49]. In FEMDEM, FEM is used to model the solid behaviour as described by continuum mechanics and switches to DEM when a fracture is generated.

2.3. Coupling methods between the fluid model (Fluidity) and solid model (Y2D)

An immersed body method is used to couple the fluid and solid models. The method was firstly presented in the work of [50]. In this approach, a thin shell mesh surrounding the solid mesh is introduced, and a coupling source term is used to calculate the exchange forces between the fluid and solid on the shell mesh. This method is capable of dealing with large displacements, open fractures and contact forces without requiring remeshing in the fluid domain.

2.3.1. Coupling equations

A supplementary equation is introduced to couple the fluid code (Fluidity) and solid code (Y2D), that is,

$$\frac{\rho_f}{\Delta t}(\hat{\boldsymbol{u}}^f - \boldsymbol{u}_f^f) = \frac{\rho_f}{\Delta t}(\boldsymbol{u}_s^s - \boldsymbol{u}_f^s), \tag{6}$$

where Δt is the time step size and $\hat{\boldsymbol{u}}^f$ is the bulk velocity ($\hat{\boldsymbol{u}}^f = b_f\boldsymbol{u}_f^f + b_s\boldsymbol{u}_s^f = \hat{\boldsymbol{u}}_f^f + \hat{\boldsymbol{u}}_s^f$, b_f and b_s being the volume fractions of the fluid and solid respectively, $b_f + b_s$=1). Subscripts denote the material fields, that is, s denotes the solid and f denotes the fluid. Superscripts denote the mesh associated with the material (s denotes values on the solid mesh and f denotes values on the fluid mesh). The solid velocity on the solid mesh $\boldsymbol{u}_s^s$ is projected onto the fluid mesh, $\hat{\boldsymbol{u}}_s^f$ [50] which is then used in the coupled system.

The coupling process is achieved by introducing a source term $\boldsymbol{s}_c$ into the momentum equation (3), which represents the effects of forces of the solid on the fluid. The momentum equation (3) then has the form of:

$$\frac{\partial}{\partial t}(\rho\mathbf{u}) + \nabla\cdot(\rho\mathbf{u}\mathbf{u} - \sigma) \quad = \quad \rho\mathbf{F} + \boldsymbol{s}_c. \tag{7}$$

The source term $\boldsymbol{s}_c$ considers an exchange of forces between the solid and fluid, and has the form $\boldsymbol{s}_c = (\boldsymbol{s}_{c,x}^f, \boldsymbol{s}_{c,y}^f, \boldsymbol{s}_{c,z}^f)^T$. For additional details, see [51].

The continuity equation has the form of,

$$\nabla\cdot\hat{\boldsymbol{u}}^f = 0, \tag{8}$$

where

$$\hat{\boldsymbol{u}}^f = \begin{cases} \boldsymbol{u}_f^f & \text{if } b_f = 1, b_s = 0 \\ \boldsymbol{u}_s^f & \text{if } b_f = 0, b_s = 1. \end{cases} \tag{9}$$

2.3.2. Coupling source term

The coupling process involves the calculation of the source term $\boldsymbol{s}_c$ in Equation (7), which is described briefly here (for additional details, see [51]). The viscosity forces $\boldsymbol{F}^s_{viscosity}$ and $\boldsymbol{F}^s_{pressure}$ are calculated by:

$$\boldsymbol{F}^s_{viscosity} + \boldsymbol{F}^s_{pressure} = \int_{\Gamma_{solid}} N\boldsymbol{n} \cdot (\underline{\underline{\tau}}_{solid} + Ip) d\Gamma, \tag{10}$$

where N is the finite element shape function, $\underline{\underline{\tau}}_{solid}$ is the viscous stress term; Γ_{solid} is the solid surface, $\boldsymbol{n}$ is the unit normal vector on the solid surface $\boldsymbol{n} = (n_x, n_y, n_z)$. I is the identity matrix and has a size of number of nodes on the solid mesh.

Once obtaining $\boldsymbol{F}^s_{viscosity}$ and $\boldsymbol{F}^s_{pressure}$, the velocity of solids $\boldsymbol{u}_s$=(u_s, v_s, w_s) can be calculated by Equation (5). The source term can then be obtained using the following equations:

$$\begin{aligned} \boldsymbol{s}^f_{c,x} &= a_{xx}u_s + a_{xy}v_s + a_{xz}w_s, \\ \boldsymbol{s}^f_{c,y} &= a_{yx}u_s + a_{yy}v_s + a_{yz}w_s, \\ \boldsymbol{s}^f_{c,z} &= a_{zx}u_s + a_{zy}v_s + a_{zz}w_s, \end{aligned} \tag{11}$$

where a denotes the viscosity coefficients and the subscript x, y and z denote the coordinate directions, Δx_{wall} is the fluid element length scale around the wall. Δr is the thickness of the shell, which is an intermediate thin area between the fluid and solid, and is introduced for calculating the impact of the solid on the fluid [50].

2.4. Fracture modelling

The fracture model used here is based on the finite-discrete element method (FEMDEM) and treats the whole domain as a multi-body system. The finite element formulation is used to model continuum behaviour (*i.e.* calculation of stress and strain) before fractures are generated. If the failure criterion is met, the discrete element formulation is then used for modelling discontinuum behaviour (contact forces and their distribution on nodes). The combination of the finite element formulation and joint element (Figure 1c) formulation ensures the transition from continuum behaviour to discontinuum behaviour can be captured accurately. The combined single and smeared crack model with the Mohr-Coulomb failure criterion is used.

The overall fracture modelling algorithm, based on FEMDEM, is given in Algorithm 1 (for details, see [49, 52]), where u^t_{solid} denotes the solid velocity vector at each node at time t, $u_{acceleration}$ is the acceleration, $f_{external}$ and $f_{internal}$ are the external and internal forces at each node respectively, and $mass$ denotes the nodal mass.

In fracture modelling, triangular and joint elements are introduced, as shown in Figure 1. The figure shows two 2-D solid discontinuous elements with an inserted 4-noded joint element. The solid domain is firstly discretised by numerous 3-noded triangular elements, and those elements are treated as input data for the fracture modelling described in Algorithm 1. A 4-noded joint element is then inserted between two triangular elements, and the stresses are calculated using FEM. The new fractures are judged by the Mohr-Coulomb criterion with a tension cut-off, see Figure 2. When the

Algorithm 1: Fracturing simulation

(1) Input data (discontinuous solid meshes).
(2) Insert 4-noded joint elements between 3-node triangular elements, see Figure 1.
(3) Calculate stresses using the finite element formulation.
(4) Judge whether the new fractures are generated using the Mohr-Coulomb failure criterion.
if new fractures are generated **then**
  add new contact couples.
else
  detect contact couples in the DEM domain.
end if
(5) Calculate contact forces in DEM domain.
(6) Calculate velocity at each node through the explicit time integration.
$u_{solid}^{t+1} = u_{solid}^{t} + u_{acceleration}\Delta t$
$u_{acceleration} = \frac{f_{external} - f_{internal}}{mass}$
(7) Output data.
(8) Goto step (3): calculate stresses using the finite element formulation.
(9) Stop.

normal stress is less than the tensile strength, the shear stress in a joint element can be expressed by Equation (12) [49].

$$\tau = c + \sigma tan\phi, \qquad \sigma_n < f_t, \tag{12}$$

where σ is the normal stress, ϕ is the internal friction angle, f_t is the tensile strength and c is the cohesion.

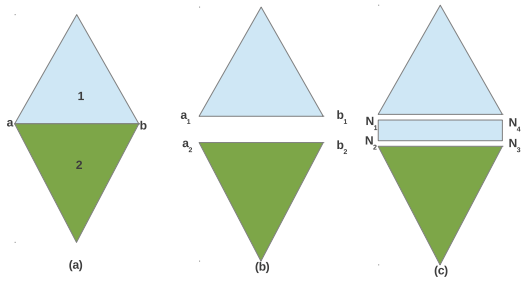

Figure 1: A 2-D solid discontinuous element with a 4-node joint element.

3. Model reduction

In this section, a NIROM is used for modelling compressible fluid flows. The high fidelity model includes the interaction between solid and compressible fluid flows as well as crack initiation and propagation. Recently there have been a number of

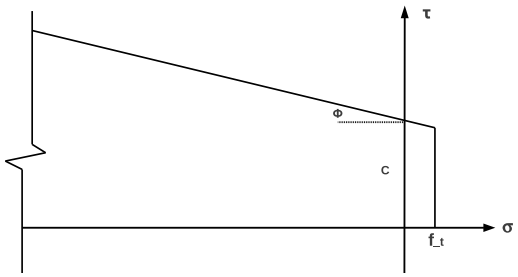

Figure 2: A Mohr-Coulomb failure criterion with a tension cut-off.

papers on reduced order modelling of compressible fluids, *e.g.* with shock waves [2, 53, 54, 55, 56, 57, 58, 59]. Most of existing ROMs for shock waves use the Galerkin (or Petrov-Galerkin) projection and POD approaches to generate the reduced order models. The challenge in using POD ROMs for shock waves is to represent the shock front (moving discontinuities). Fang *et al.* [2] introduced a Petrov-Galerkin approach for dealing with sharp or abrupt field changes in discontinuous Galerkin reduced order modelling. Lucia [57] proposed a domain decomposition approach that isolates the region containing the moving shock wave for special treatment. The Gauss-Newton method with approximated tensors [56] and the clustering Algorithm [59] were also developed for accurately capturing the shock front. In this work, a non-intrusive ROM using RBF is proposed for modelling the resulting abruptly changing (in space and time) fields. The POD basis functions are generated from solution snapshots where the details of the crack patterns (through the volume fraction and velocity of the solids) as well as the fluid velocity/pressure/density are included. The accuracy of the coupling NIROM results is sensitive to the number of solution snapshots chosen because of the rapidly changing fields. Due to the dissipative properties of RBF's representation of dynamics with NIROM, the numerical oscillations associated with POD intrusive methods that use Bubnov-Galerkin methods are reduced.

In reduced order modelling, any variable can be expressed as a linear combination of a number of POD basis functions representing the original high fidelity modelling system in an optimal sense. It has the following form:

$$\varphi = \overline{\varphi} + \sum_{i=1}^{m} \alpha_i \Phi_i, \tag{13}$$

where φ denotes a variable to be solved (*e.g.* the velocity, pressure, density and solid concentration), $\overline{\varphi}$ is the mean of variable solutions over the simulation time period, α denotes the POD coefficients, m is the number of POD basis functions and Φ denotes the POD basis functions. Using POD, the basis functions can be calculated from snapshots of variable solutions recorded at regular time intervals. The radial basis function interpolation method is used to calculate the POD coefficients. The procedure of POD is summarized in Algorithm 2.

The radial basis function interpolation is used to determine the POD coefficients in (13). Commonly used RBFs are plate spline, multi-quadric, inverse multi-quadric and

Algorithm 2: Proper Orthogonal Decomposition

(1) Compute solution of the coupled compressible fluid and solid system at time levels 1, ..., N_s ;

(2) Retrieve the snapshots matrix A from the solutions obtained;

(3) Subtract the mean of snapshots matrix A, *i.e.* $A' = A - A_{mean}$;

(4) Perform Singular Value Decomposition (SVD) to snapshots matrix A or A', *i.e.* $A = E\Sigma F^T$;

(5) Choose the dimension of ROM, m ($m < N_s$);

(6) Obtain the POD basis functions $\Phi_i = E_{:,i}$, for $i \in \{1, 2 \dots m\}$;

Gaussian. RBFs have been widely used in the context of multidimensional interpolation. An interpolation function $f(x)$ representing a physical problem can be approximated through a linear combination of the RBF ϕ centred at N points. In this work, the Gaussian RBF is used to construct the interpolation function $f(x)$. The Gaussian RBF has a form of $\phi(r) = e^{-(r/\zeta)^2}$ (r being the radius and ζ being the shape parameter).

In the following paragraph, a set of interpolation functions or hypersurfaces is derived through the POD-RBF method. The POD-RBF NIROM was first presented by Xiao *et al.* [37]. In this work this method is used to derive NIROM for the compressible fluid and fractured solid problem. The formulation of the POD-RBF NIROM is:

$$\alpha^n_{\mathbf{z},j} = f_{\mathbf{z},j}(\alpha^{n-1}_{\mathbf{u}}, \alpha^{n-1}_p, \alpha^{n-1}_d, \alpha^{n-1}_c), \tag{14}$$

where α denotes POD coefficients, subscripts $\mathbf{u}$, p, d and c denote velocity, pressure, density and solid concentration components respectively, $\mathbf{z}$ denotes one of the variables ($\mathbf{u}$, p, d and c), subscript j is the j^{th} POD coefficient of a complete set of POD coefficients ($\alpha_{\mathbf{u}}, \alpha_v, \alpha_d, \alpha_c$), n is the time level, f is a set of hypersurfaces representing the reduced order dynamical system.

The hypersurface functions are constructed using the POD-RBF method, as described in Algorithm 3, where N denotes the number of data points ($\boldsymbol{\alpha}^1, \boldsymbol{\alpha}^2, \cdots, \boldsymbol{\alpha}^N$, where $\boldsymbol{\alpha} = \alpha_{\mathbf{u}}, \alpha_p, \alpha_d, \alpha_c$) and A is the matrix associated with the data point and centre $\mathbf{c}$ and $A_{i,j} = \phi(\left\|(\alpha^j_{\mathbf{u}}, \alpha^j_p, \alpha^j_d, \alpha^j_c) - \mathbf{c}^i\right\|)$, $i, j \in \{1, 2 \dots N\}$. The centre $\mathbf{c}$ is chosen to be the origin of the input data.

The online NIROM calculation for coupling of compressible fluid and fractured solid problems is described in Algorithm 4. In the high-fidelity model, the solid-fluid movement is fully coupled, as explained in Section 2. The coupling results are recorded and stored in the snapshots where the details of the fracture patterns (through the volume fraction and velocity of the solids) as well as the fluid velocity/pressure/density are included. The high-fidelity solutions on the solid mesh are interpolated onto the fluid mesh and then stored in the snapshots. The POD basis functions are then generated

Algorithm 3: Constructing a set of hypersurface using POD-RBF

(1) Generate a number of snapshots over the time period $[0, T]$ by solving the compressible fluid/solid coupling problem and fracture model;

(2) Calculate POD basis functions $\Phi_{\mathbf{u}}$, Φ_p, Φ_d and Φ_c through a truncated SVD of the snapshots matrix;

(3) Obtain the functional values $y_{i,j}$ at the data point $\alpha_{\mathbf{u}}^i, \alpha_p^i, \alpha_d^i, \alpha_c^i$ via the solutions from the high fidelity full model, where $i \in \{1, 2, \ldots N\}$ and $j \in \{1, 2, \ldots m\}$;

(4) Obtain a set of hypersurfaces through the following loop:

for $j = 1$ *to* m **do**

(i) Calculate the weights $\mathbf{w}_{i,j}$ by solving Equation (15);

$$A\mathbf{w}_{i,j} = y_{i,j}, \quad i \in \{1, 2, \ldots, N\}, \tag{15}$$

(ii) Obtain a set of hyper surfaces ($f_{\mathbf{u},j}$, $f_{p,j}$, $f_{d,j}$, $f_{c,j}$) by substituting the weight values obtained in the above step into Equation (16);

$$f_{\mathbf{z},j}(\alpha_{\mathbf{u}}, \alpha_p, \alpha_d, \alpha_c) = \sum_{i=1}^{N} w_{i,j}\phi_j(\left\|(\alpha_{\mathbf{u}}, \alpha_p, \alpha_d, \alpha_c) - (\alpha_{\mathbf{u}}^i, \alpha_p^i, \alpha_d^i, \alpha_c^i)\right\|), \tag{16}$$

endfor

from the snapshots and used to construct the NIROM for coupling of fluid and solid problems. Thus, the solids volume fractions and solids velocity are calculated within the NIROM. The accuracy of the coupling NIROM results is dependent on the number of snapshots chosen.

Algorithm 4: Online NIROM calculation for compressible fluid and fractured solid problems

(1) Initialisation.
for $j = 1$ *to* m **do**
Initialize $\alpha^0_{\mathbf{u},j}$, $\alpha^0_{p,j}$, $\alpha^0_{d,j}$ and $\alpha^0_{c,j}$;
endfor

(2) Calculate solutions at current time level:
for $n = 1$ *to* T **do**
for $j = 1$ *to* m **do**
Solving fluid process:

(i) Evaluate the hypersurfaces f at previous time level $n-1$ by using the complete set of POD coefficients $\alpha^{n-1}_{u,j}$, $\alpha^{n-1}_{p,j}$, $\alpha^{n-1}_{d,j}$ and $\alpha^{n-1}_{c,j}$:

$$f_{\mathbf{z},j} \leftarrow (\alpha^{n-1}_{\mathbf{u}}, \alpha^{n-1}_{v}, \alpha^{n-1}_{d}, \alpha^{n-1}_{c}),$$

(ii) Calculate the POD coefficients $\alpha^n_{\mathbf{u}}$, α^n_p, α^n_d and α^n_c at current time level n using the following equations:

$$\alpha^n_{\mathbf{z},j} = \sum_{i=1}^{N} w_{i,j}\phi_{i,j}(r),$$

endfor

Calculate the solution $\mathbf{u}^n$, p^n, d^n and c^n on the full space at current time level n by projecting $\alpha^n_{\mathbf{u},j}$, $\alpha^n_{p,j}$, $\alpha^n_{d,j}$ and $\alpha^n_{c,j}$ onto the full space.

$$\mathbf{u}^n = \sum_{j=1}^{m} \alpha^n_{\mathbf{u},j}\Phi_{\mathbf{u},j}, \quad p^n = \sum_{j=1}^{m} \alpha^n_{p,j}\Phi_{p,j}, \quad d^n = \sum_{j=1}^{m} \alpha^n_{d,j}\Phi_{d,j}, \quad c^n = \sum_{j=1}^{m} \alpha^n_{c,j}\Phi_{c,j},$$

.
endfor

4. Application to compressible fluid and fractured solid problem

The NIROM has been implemented under the framework of an advanced unstructured mesh multi-phase fluid model (Fluidity) and a combined finite-discrete element method based solid model (Y2D). The NIROM is first validated using an immersed wall in a fluid, then further validated using a more complex blasting example problem.

4.1. Case 1: an immersed wall in a fluid

The first case is an immersed wall in a fluid test case [43]. In this case, a solid beam is embedded in a fluid and is subject to a pressure wave. The domain consists of a rectangle of non-dimensional size of 4×2 with 7500 nodes and 2500 elements. The beam is located at the bottom center and has a size of 0.286×1. The area ($0 < x < 1.5$) has a non-dimensional density of 8 and an initial pressure of 516.5. The rest of the domain has a density of 1.5 and an initial pressure of 1. A slip boundary condition is applied on the left, bottom and the top sides. The open boundary condition is applied on the right side. The density of the solid is 100.

The high fidelity full model was simulated during the time period $[0, 0.8]$ with a time step size of $\Delta t = 0.001$. 800 snapshots were taken at a regularly spaced time interval of 0.001. From these snapshots, the POD basis functions were formed in two ways: either subtracting the mean of snapshots or not before the singular value decomposition (SVD) is performed.

4.1.1. Case 1a: NIROM constructed with mean subtracted before constructing the POD basis functions

The NIROM was first formed with the mean snapshot solution subtracted from the snapshots before constructing the POD basis functions, see Equation 13. In this case, 30 POD basis functions representing almost 99.5% of energy in the original dynamical system were chosen to form the NIROM. The logarithm of the singular eigenvalues of velocity, pressure, density and solid concentration associated with the 30 POD basis functions are presented in Figure 3.

The pressure and velocity results from both the high fidelity model and the NIROM are shown in Figures 4 and 5 respectively. It is seen here that these NIROM results are not in good agreement with the high fidelity model. The root mean square error (RMSE) and correlation coefficient between the high fidelity model and the NIROM are shown in Figure 6. It can be seen that the RMSE of the NIROM results is around 39.59 while the correlation coefficient is mostly less than 0.6. The RMSE reflects the differences of the two models. Both the RMSE and the correlation coefficient suggest that the NIROM is not in good agreement with the high fidelity model. This is further shown by comparison of the NIROM with the high fidelity model pressure (Figure 4) and velocity (Figure 5) distributions. This is also reflected by the correlation coefficient curve, which varies significantly with time. The accuracy of NIROM results therefore, is low and needs to be improved. We also plot the correlation coefficient and RMSE obtained using a POD basis calculated from the snapshot matrix $[x_0 - \bar{x};\ x_1 - \bar{x};\ ...;\ x_N - \bar{x}, \bar{x}]$, in which the last column of the snapshot matrix contains the mean solution. Figure 7 shows the RMSE and correlation coefficient between the high fidelity and the NIROM with 12, 18 and 30 POD basis functions.

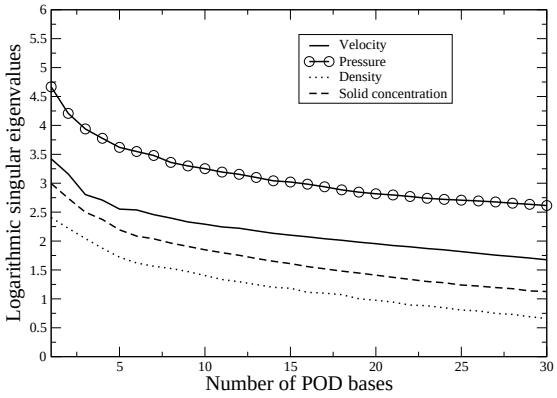

Figure 3: Case 1a: the figure shows the logarithm of the singular eigenvalues of velocity, pressure, density and solid concentration in order of decreasing magnitude, where the mean is subtracted from the snapshots before constructing the POD basis functions.

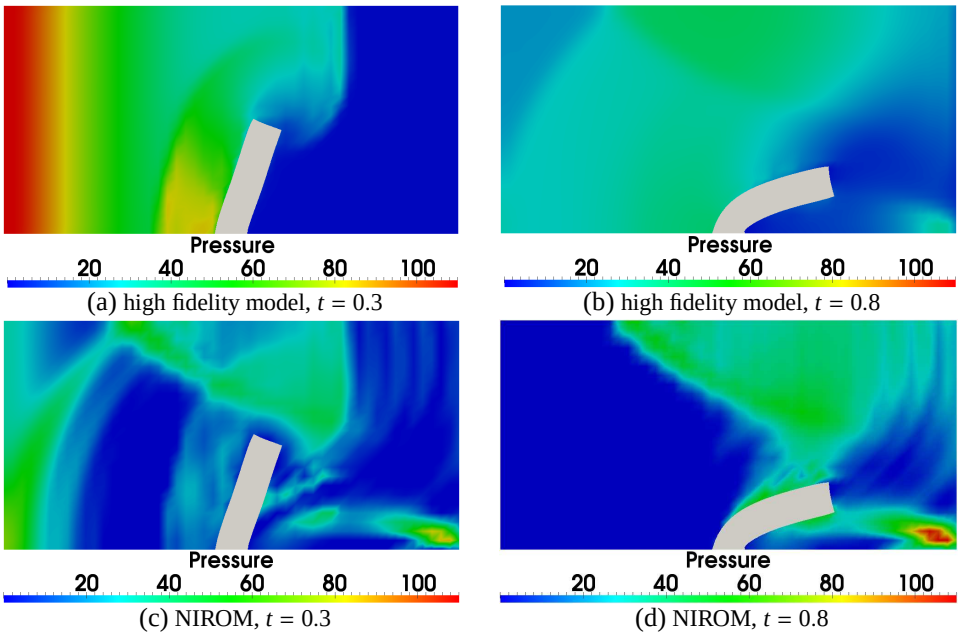

(a) high fidelity model, $t = 0.3$ (b) high fidelity model, $t = 0.8$

(c) NIROM, $t = 0.3$ (d) NIROM, $t = 0.8$

Figure 4: Case 1a: comparison of pressure solutions between the high-fidelity full model and NIROM using 30 POD basis functions at time instances $t = 0.3$ and $t = 0.8$. The mean is subtracted from the snapshots before constructing the POD basis functions.

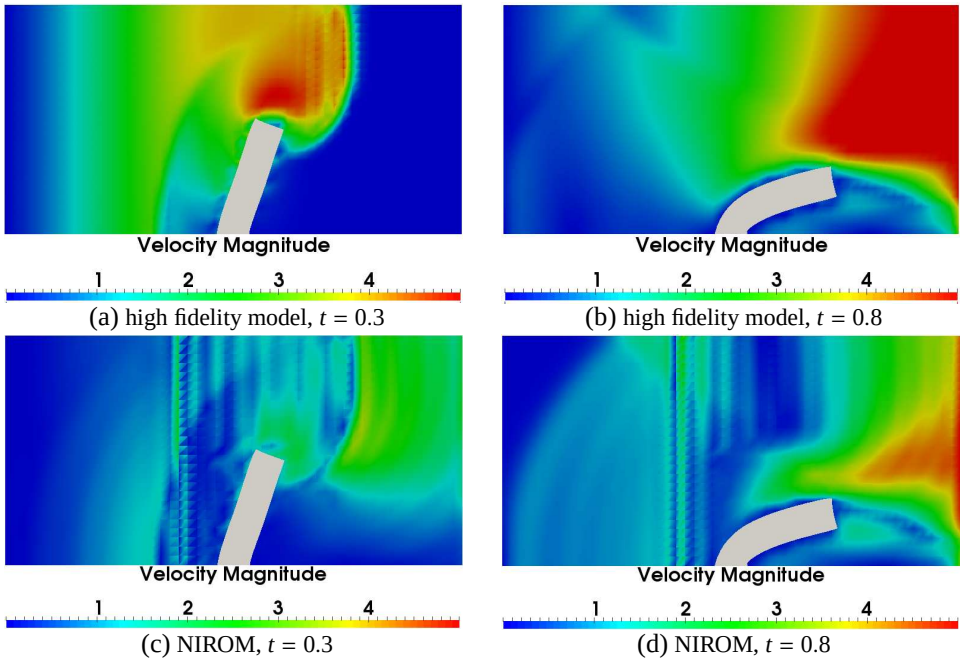

(a) high fidelity model, $t = 0.3$ (b) high fidelity model, $t = 0.8$

(c) NIROM, $t = 0.3$ (d) NIROM, $t = 0.8$

Figure 5: Case 1a: comparison of velocity solutions between the high-fidelity full model and NIROM using 30 POD basis functions at time instances $t = 0.3$ and $t = 0.8$. The mean is subtracted from the snapshots before constructing the POD basis functions.

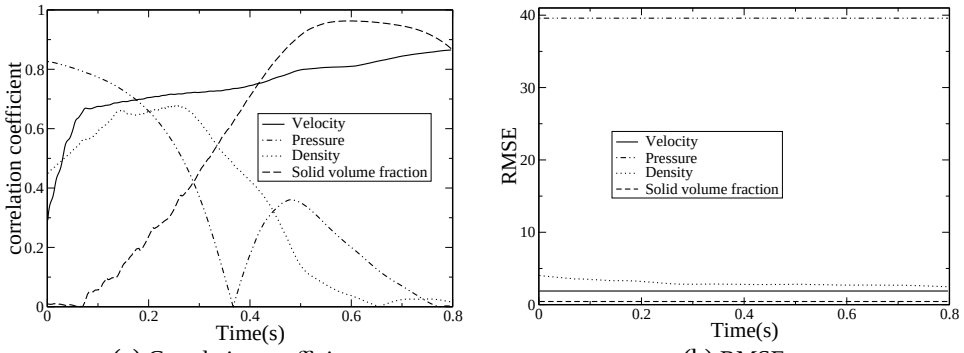

(a) Correlation coefficient (b) RMSE

Figure 6: Case 1a: the correlation coefficient and RMSE of pressure solutions between the high fidelity and NIROM using 30 POD basis functions. The mean is subtracted from the snapshots before constructing the POD basis functions.

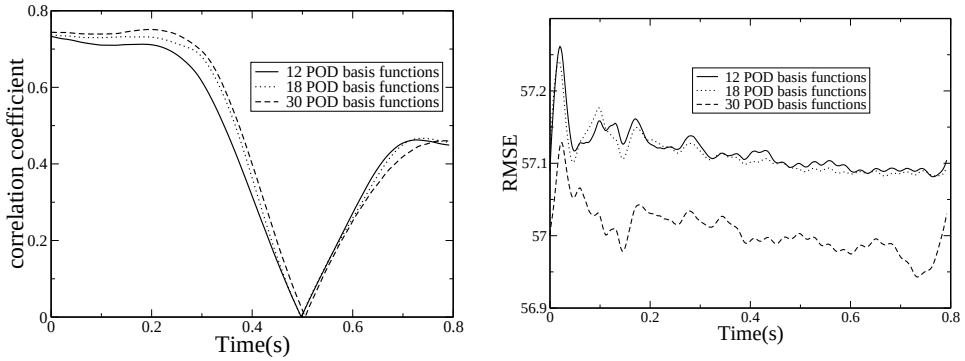

(a) Correlation coefficient (b) RMSE

Figure 7: Case 1: RMSE and correlation coefficient between the high fidelity and fluid and NIROM with 12, 18 and 30 POD basis functions, where the mean is put at the end of snapshot matrix.

4.1.2. *Case 1b: NIROM constructed with mean not subtracted before constructing the POD basis functions*

In this subsection, the NIROM constructed with mean not subtracted before constructing the POD basis is applied. Figure 8 presents the logarithm of the singular eigenvalues of velocity, pressure, density and solid concentration in order of decreasing magnitude.

Figure 9 shows a comparison of pressure solutions between the high-fidelity full model and NIROM using 12, 18 and 30 POD basis functions at time instances $t = 0.3$ and $t = 0.8$. We can see that the results from the NIROM are in agreement with those from the high fidelity model. The front is captured well, even when only 12 POD basis functions are used. The accuracy of NIROM results is improved with the increased in number of POD basis functions. The absolute error of pressure solutions between the high fidelity model and NIROM using different numbers of POD basis functions at time instances $t = 0.3$ and $t = 0.8$ is given in Figure 11. The figure clearly shows that the error of the NIROM relative to the high fidelity model becomes smaller as the number of POD basis functions is increased. The velocity solutions from both the high fidelity model and the NIROM with 30 POD basis functions at time instances $t = 0.3$ and $t = 0.8$ are given in Figure 10.

To further validate the accuracy of the NIROM with mean not subtracted, the correlation coefficient and RMSE of pressure results between the high fidelity model and NIROM are used for error analysis, see Figure 11. It is shown that the correlation coefficient is larger than 0.9955, while the RMSE is smaller than 2 when 12 POD basis functions are used. The error is further decreased as the number of POD basis functions is increased. It is shown that the accuracy of NIROM results is improved when the mean of snapshots is not subtracted before performing the SVD process (Figure 11). The correlation coefficient increases from 0.4 to 0.9955 while the RMSE decreases from 39.6 to 2 in comparison with results shown in Figure 6.

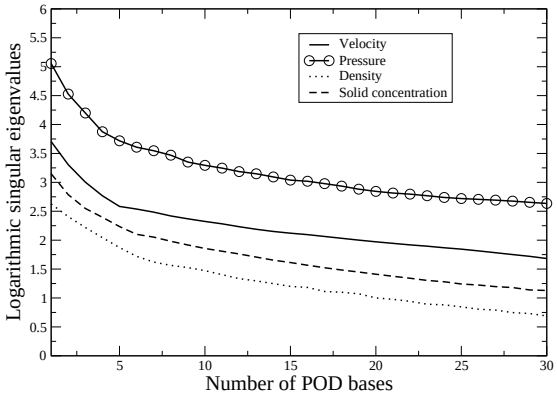

Figure 8: Case 1b : the figure shows the logarithm of the singular eigenvalues of velocity, pressure, density and solid concentration in order of decreasing magnitude. The mean is not subtracted from the snapshots before constructing the POD basis functions.

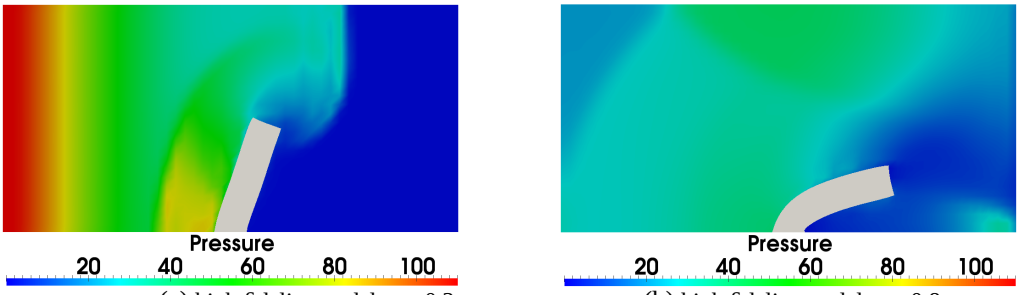

(a) high fidelity model, $t = 0.3$ (b) high fidelity model, $t = 0.8$

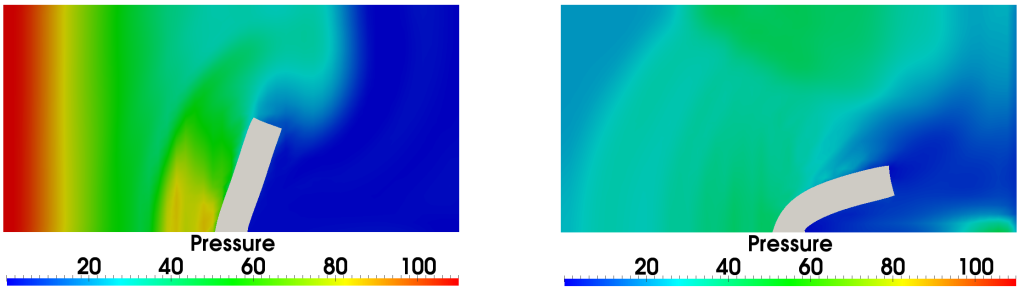

(c) NIROM (12 POD basis functions), $t = 0.3$ (d) NIROM (12 POD basis functions), $t = 0.8$

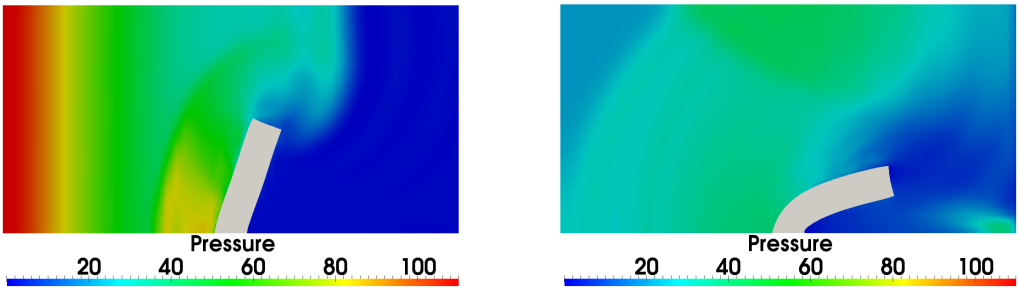

(e) NIROM (18 POD basis functions), $t = 0.3$ (f) NIROM (18 POD basis functions), $t = 0.8$

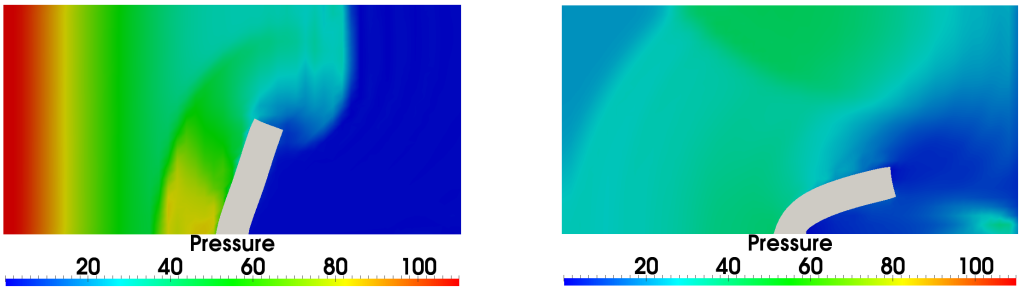

(g) NIROM (30 POD basis functions), $t = 0.3$ (h) NIROM (30 POD basis functions), $t = 0.8$

Figure 9: Case 1b: comparison of pressure solutions between the high-fidelity full model and NIROM with 12, 18 and 30 POD basis functions at time instances $t = 0.3$ and $t = 0.8$. The mean is not subtracted from the snapshots before constructing the POD basis functions.

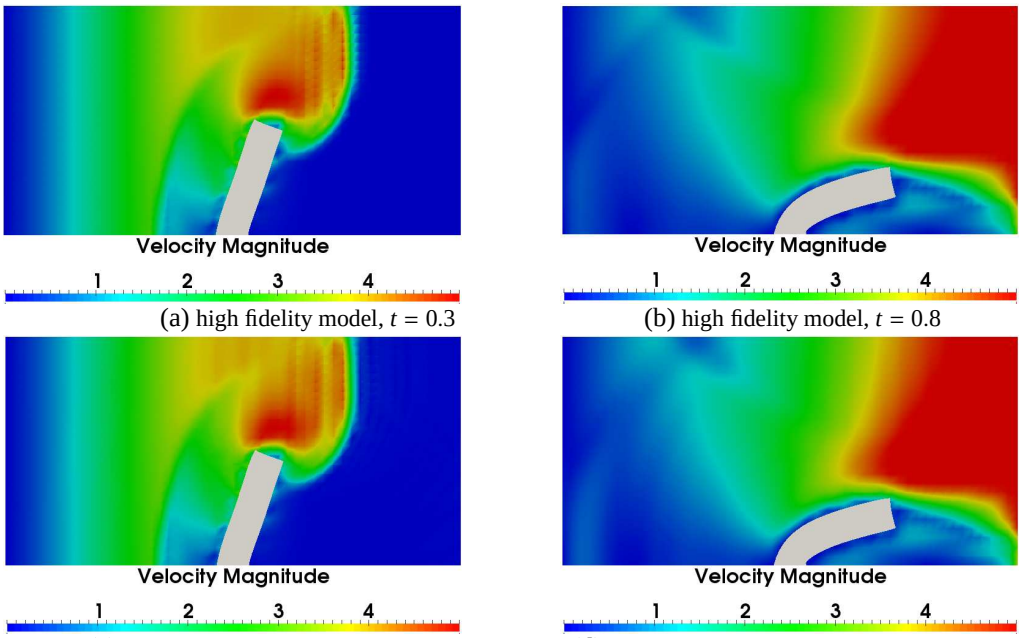

(a) high fidelity model, $t = 0.3$ (b) high fidelity model, $t = 0.8$

(c) NIROM (30 POD basis functions), $t = 0.3$ (d) NIROM (30 POD basis functions), $t = 0.8$

Figure 10: Case 1b: comparison of velocity solutions between the high-fidelity full model and NIROM with 30 POD basis functions at time instances $t = 0.3$ and $t = 0.8$. The mean is not subtracted from the snapshots before constructing the POD basis functions.

The relative errors (RE) of the four variables for both NIROMs, with and without subtracting out the mean from the snapshots, are listed in Table 1. The relative initial error is defined by the initial error divided by the values of nodes at the last time level. The calculation formula considering all nodes is given below:

$$RE = \frac{\sum_{i=1}^{N_{nodes}} ({\varphi_0}^i - \Phi\Phi^T {\varphi_0}^i)^2}{\sum_{i=1}^{N_{nodes}} {\varphi_0}^i}, \tag{17}$$

where N_{nodes} is the number of nodes on the mesh and RE is the relative initial errors to the values of nodes at the first time level. φ_0 is the initial solution of the high-fidelity full model for four variables.

It is seen in Table 1 that the relative initial error in the NIROM constructed with the mean subtracted from the snapshots is between 45-120 times larger than that from the NIROM constructed with the mean not subtracted from the snapshots.

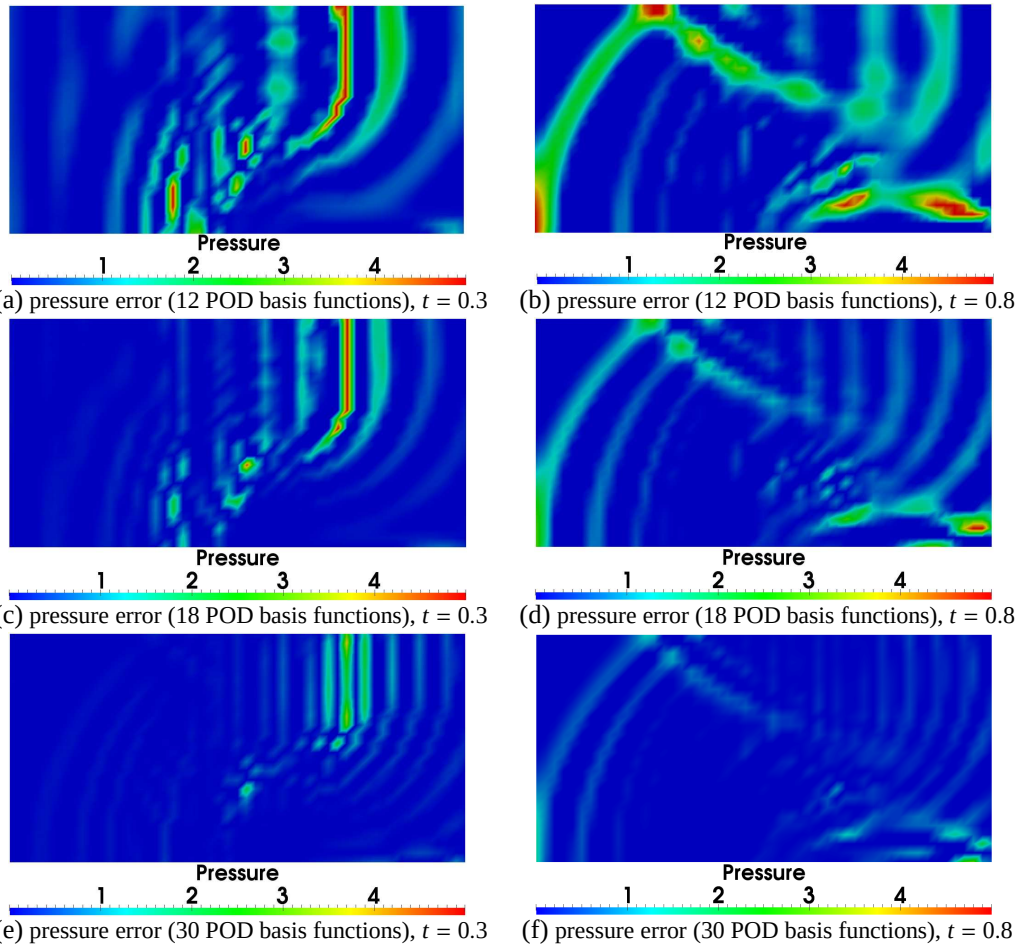

(a) pressure error (12 POD basis functions), $t = 0.3$ (b) pressure error (12 POD basis functions), $t = 0.8$

(c) pressure error (18 POD basis functions), $t = 0.3$ (d) pressure error (18 POD basis functions), $t = 0.8$

(e) pressure error (30 POD basis functions), $t = 0.3$ (f) pressure error (30 POD basis functions), $t = 0.8$

Figure 11: Case 1b: pressure error between the high fidelity model and NIROM with 12, 18 and 30 POD basis functions at time instances $t = 0.3$ and $t = 0.8$. The mean is not subtracted from the snapshots before constructing the POD basis functions.

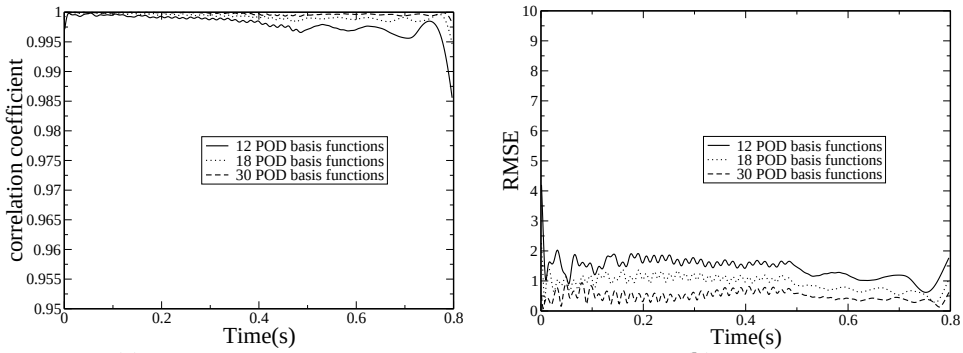

(a) Correlation coefficient (b) RMSE

Figure 12: Case 1b: RMSE and correlation coefficient of pressure solutions between the high fidelity and NIROM with 12, 18 and 30 POD basis functions. The mean is not subtracted from the snapshots before constructing the POD basis functions.

Table 1: Case 1: comparison of relative initial errors for four variables between the NIROM with mean subtracted (case 1a) and NIROM with mean not subtracted (case 1b).

Variable errors	case 1a %	case 1b %	nodes	basis functions
velocity	0.159	0.0088	7500	30
pressure	1.76	0.0149	7500	30
density	1.41	0.0141	7500	30
solid volume fraction	0.11	0.0025	7500	30

4.2. Case 2: blasting test case

To demonstrate the capability of the NIROM, the model is further applied to a highly nonlinear blasting-induced fracture test case. The computational domain is presented in Figure 13, which includes a solid square $2\,m \times 2\,m$ block embedded within a compressible gas rectangle area with a size of $3 \times 3\,m$. The highly energetic initial area lies at the center of the computational domain with a diameter of $0.2\,m$ and has a very high initial pressure. The initial high pressure of the energetic area is set to be $10^8\,Pa$ and the initial high temperature is $1000\,Kelvin$. The background area (excluding the explosion point) has an initial pressure of $101325\,Pa$ and an initial temperature of $273.26\,Kelvin$. The viscosity μ is $0.1\,Pa{\cdot}s$, the solid has a density of $2340\,kg/m^3$ and has a penalty number of 2.0×10^{10} and a Youngs modulus E of 2.66×10^{10}. The tensile and the shear strengths are $4 \times 10^6\,Pa$ and $1.4 \times 10^7\,Pa$ respectively and the energy release rate is $200\,N/m$.

The high fidelity model was simulated with a finite element mesh of 48600 nodes and 16200 elements during the time period $[0, 0.2]\,s$ with a time step size of $\Delta t = 8 \times 10^{-5}\,s$. 250 snapshots were taken at regular time intervals of $\Delta t = 8 \times 10^{-4}\,s$. The temperature solutions solved by the energy equation at time levels $t = 0.04\,s$ and $t = 0.16\,s$ are given in Figure 14.

4.2.1. Case 2a: NIROM solutions with mean subtracted before constructing the POD basis functions

In this section, the results from NIROM with the mean snapshot solution subtracted from the snapshots before constructing the POD basis functions are presented. Figure 15 shows the logarithm of the singular eigenvalues of velocity, pressure, density and solid concentration in order of decreasing magnitude. Figure 16 presents the velocity solutions from the high fidelity model and NIROM with 100 POD basis functions at time instances $t = 0.04\,s$ and $t = 0.16\,s$. It is shown that the structure of flows obtained from the NIROM is similar to that from the high fidelity model, but there are some large errors in velocity values. Figure 17 shows the pressure solutions from the high fidelity model and NIROM with 100 POD basis functions at time instances $t = 0.04\,s$ and $t = 0.16\,s$. It is seen that there is a large error in the NIROM results. This is caused by the large error in the initial conditions. We found the error in the initial pressure from the NIROM with mean subtracted from snapshots is about 1000 times larger than that of the NIROM with mean not subtracted.

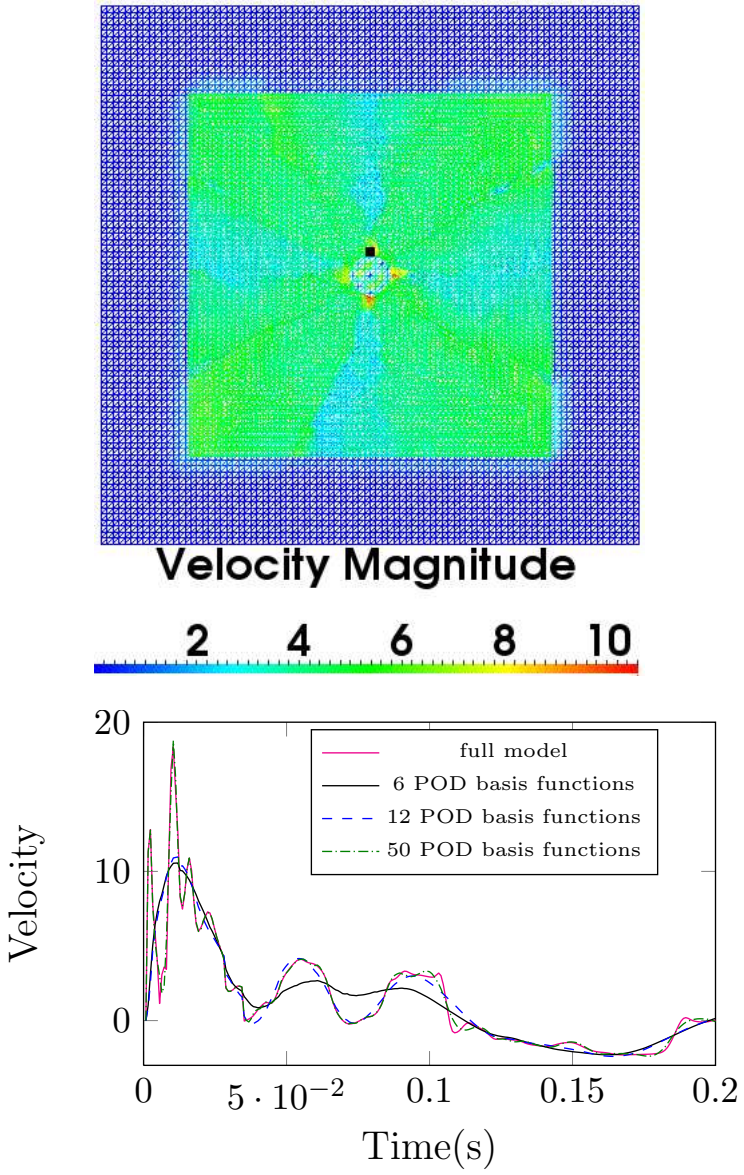

Figure 13: Case 2b: velocity comparison at a point ($x = 1.5\,m, y = 1.6333\,m$). The mean is not subtracted from the snapshots before constructing the POD basis functions.

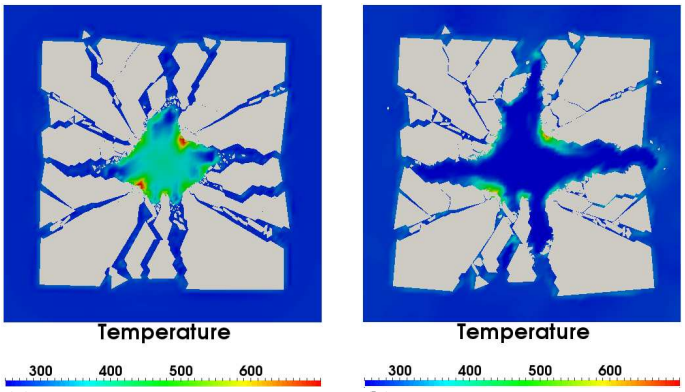

(a) high fidelity model, $t = 0.04\ s$ (b) high fidelity model, $t = 0.16\ s$

Figure 14: Case 2a: temperature solutions obtained from the high-fidelity full model at time levels $t = 0.04\ s$ and $t = 0.16\ s$.

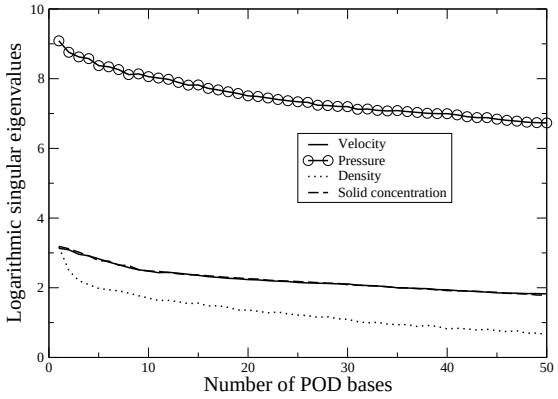

Figure 15: Case 2a: The logarithm of the singular eigenvalues of velocity, pressure, density and solid concentration in order of decreasing magnitude. The mean is subtracted from the snapshots before constructing the POD basis functions.

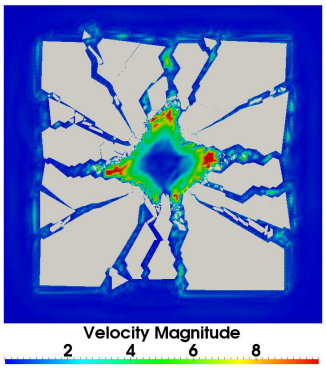

(a) high fidelity model, $t = 0.04\ s$

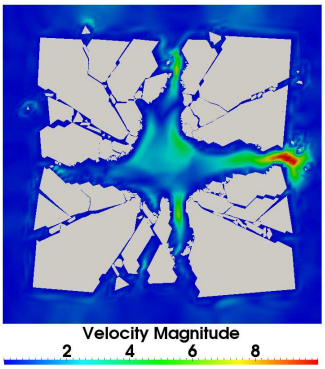

(b) high fidelity model, $t = 0.16\ s$

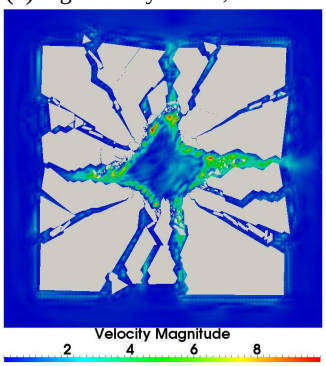

(c) (100 POD basis functions), $t = 0.04\ s$

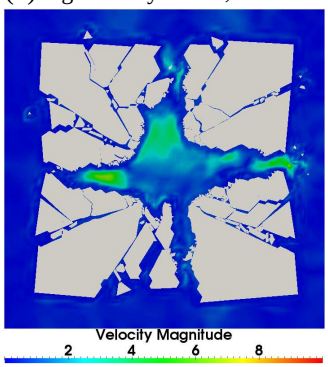

(d) (100 POD basis functions), $t = 0.16\ s$

Figure 16: Case 2a: comparison of velocity solutions between the high-fidelity model and NIROM using 100 POD basis functions at time instances $t = 0.04\,s$ and $t = 0.16\,s$. The mean is subtracted from the snapshots before constructing the POD basis functions.

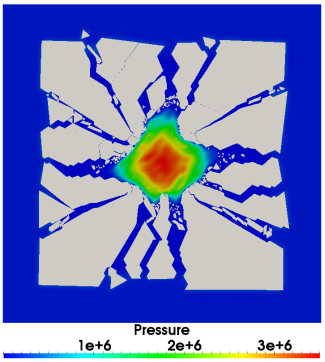

(a) high fidelity model, $t = 0.04\ s$

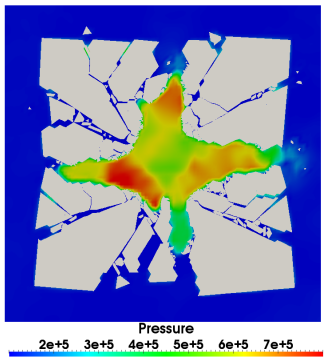

(b) high fidelity model, $t = 0.16\ s$

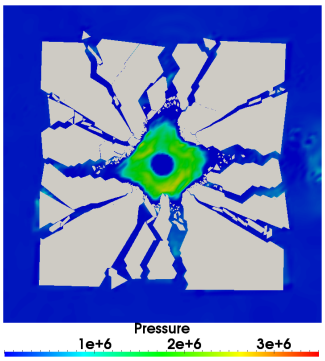

(c) NIROM (100 POD basis functions), $t = 0.04\ s$

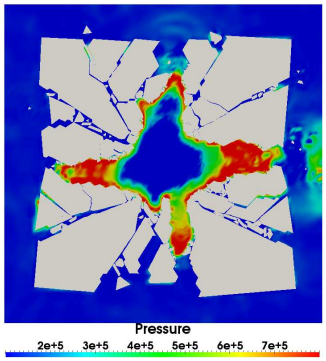

(d) NIROM (100 POD basis functions), $t = 0.16\ s$

Figure 17: Case 2a: comparison of pressure solutions between the high-fidelity model and NIROM with 100 POD basis functions at time instances $t = 0.04\ s$ and $t = 0.16\ s$. The mean is subtracted from the snapshots before constructing the POD basis functions.

4.2.2. Case 2b: NIROM solutions with mean not subtracted from snapshots before constructing the POD basis functions

In this section, the results from the NIROM with mean not subtracted from snapshots before constructing the POD basis functions are presented. Figure 18 shows the logarithm of the singular eigenvalues of velocity, pressure, density and solid concentration in order of decreasing magnitude.

Figure 19 shows a comparison of velocity solutions between the high-fidelity full model and NIROM using 6, 12 and 50 POD basis functions at time instances $t = 0.04\ s$ and $t = 0.16\ s$. It is evident that the NIROM, with only 6 POD basis functions, performs well when the mean of solution snapshots is not subtracted before constructing the POD basis functions, even better than the solutions from the NIROM with 100 POD basis functions, when the mean is subtracted before applying the SVD – as shown in Figure 16. Figure 19 also shows that the shock front of the blast wave is captured very well by increasing the number of POD basis functions from 6 to 50. There is no visible difference between the high fidelity model and NIROM with 50 POD basis functions. The difference of pressure solutions between the high fidelity model and NIROM with 6, 12 and 50 POD basis functions at time instances $t = 0.04$ and $t = 0.16\ s$ is presented in Figure 20. It is evident that a higher accuracy is obtained by choosing a larger number of POD basis functions.

Figure 21 presents a comparison of pressure solutions between the high-fidelity full model and NIROM using 6, 12 and 50 POD basis functions at time instances $t = 0.04\ s$ and $t = 0.16$. The pressure solutions from the NIROM (Figure 21) are not as good as velocity solutions from the NIROM shown in Figure 19. There are visible differences between the high fidelity model and NIROM when 6 and 12 POD basis functions are used, which is evident at the time instance $t = 0.16\ s$. The errors between the high fidelity model and NIROM with 6, 12 and 50 POD basis functions at time instances $t = 0.04\ s$ and $t = 0.16\ s$ are plotted in Figure 22. It is evident that the error is decreased by choosing more POD basis functions.

The solid volume fraction solutions obtained from the high-fidelity full model and NIROM with 50 POD basis functions are given in Figure 23. As we can see, the results from the high-fidelity model and NIROM are close to each other.

In order to further assess the performance of the NIROM, the velocity solution obtained from the high fidelity model and NIROMs at a point ($x = 1.5\,m, y = 1.6333\,m$) near the explosion point over the simulation time period is plotted in Figure 13. The reason why we choose the point around the explosion centre is that there is an abrupt change around the explosion point. Figure 13 illustrates that NIROM with a small number of POD basis functions perform well when there are no abrupt changes, whereas NIROM with 50 POD basis functions captures the abrupt changes very well.

The accuracy of the NIROM is validated by the RMSE and correlation coefficients of pressure solutions between the high fidelity model and NIROM. It is shown in Figure 24 that the RMSE of pressure results decreases as the number of POD basis functions increases. The correlation coefficients are over 0.935, indicating that the high fidelity model and NIROM are highly correlated. The NIROM has closer agreement to the high fidelity model as the number of POD basis functions increases.

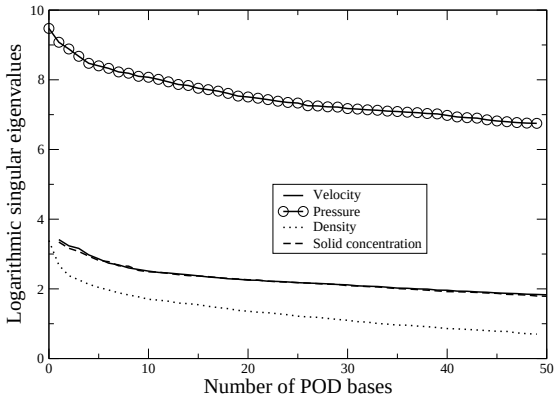

Figure 18: Case 2b: The logarithm of the singular eigenvalues of velocity, pressure, density and solid concentration in order of decreasing magnitude. The mean is not subtracted from the snapshots before constructing the POD basis functions.

4.2.3. Case 2c: Untrained blasting case

An untrained initial condition was used to demonstrate how well the NIROM could perform when the initial pressure was not part of the training simulations. The initial pressure values used in each training simulation are 258.3 Pa, 387.45 Pa, 671.58 Pa and 723.24 Pa respectively. The unseen test case has an initial pressure of 464.95 Pa. The closest training simulation to the unseen test simulation is 387.45 Pa. The pressure solutions of this closest training simulation of the high-fidelity full model (initial pressure of 387.45 Pa) and unseen test simulation of the high-fidelity full model (initial pressure of 464.95 Pa) are given in Figure 25. It is shown that the solution at $t = 0.12$ for the unseen case is quite different from that for the closest training case. Therefore, this unseen case is suitable to be used for demonstrating the predictive capability of NIROM.

Figure 26 shows the pressure and velocity solutions obtained from the high-fidelity model and NIROM with 24 POD basis functions for the unseen initial pressure condition at the time level $t = 0.12$ s. The errors of pressure and velocity solutions between the high fidelity model and NIROM are also presented in Figure 26 (e) and (f). The figure illustrates that the NIROM results are in agreement with those from the high fidelity model.

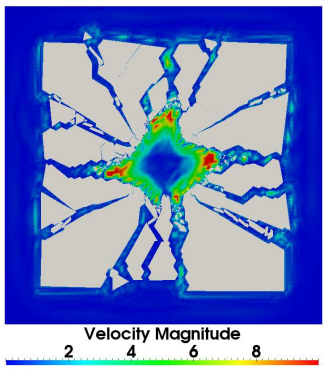

(a) high fidelity model, $t = 0.04\ s$

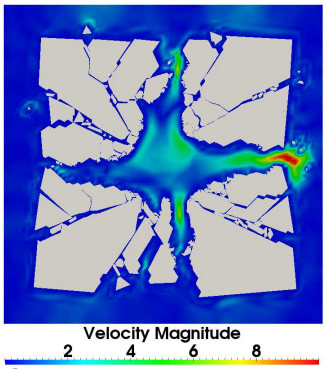

(b) high fidelity model, $t = 0.16\ s$

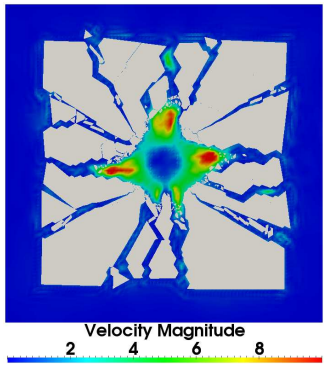

(c) NIROM (6 POD basis functions), $t = 0.04$

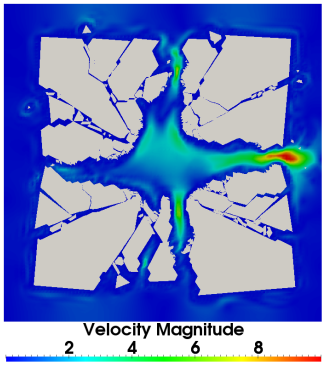

(d) NIROM (6 POD basis functions), $t = 0.16$

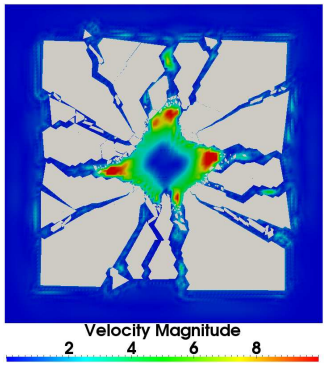

(e) NIROM (12 POD basis functions), $t = 0.04\ s$

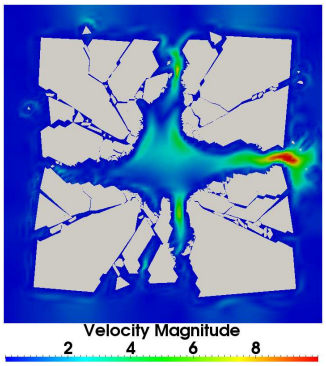

(f) NIROM (12 POD basis functions), $t = 0.16\ s$

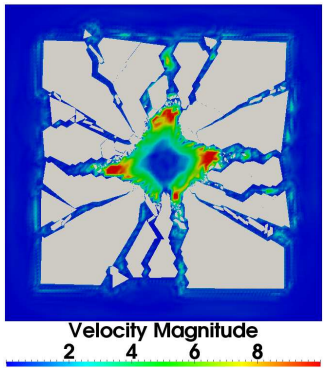

(g) NIROM (50 POD basis functions), $t = 0.04\ s$

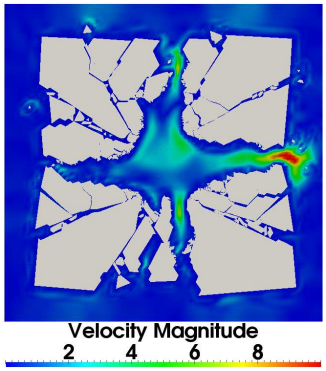

(h) NIROM (50 POD basis functions), $t = 0.16\ s$

Figure 19: Case 2b: comparison of velocity solutions between the high-fidelity model and NIROM with 6, 12 and 50 POD basis functions at time instances $t = 0.04\ s$ and $t = 0.16\ s$. The mean is not subtracted from the snapshots before constructing the POD basis functions.

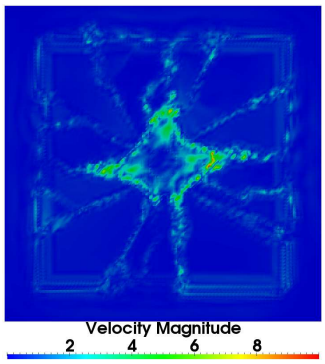

(a) error (6 POD basis functions), $t = 0.04\,s$

(b) error (6 POD basis functions), $t = 0.16\,s$

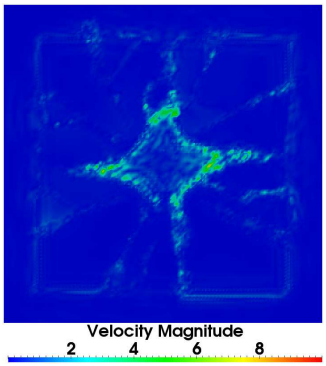

(c) error (12 POD basis functions), $t = 0.04\,s$

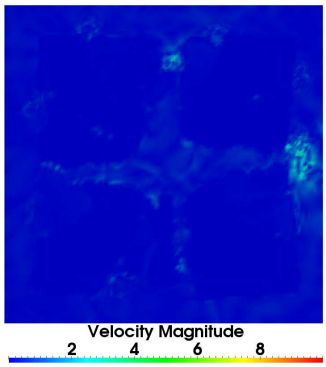

(d) error (12 POD basis functions), $t = 0.16\,s$

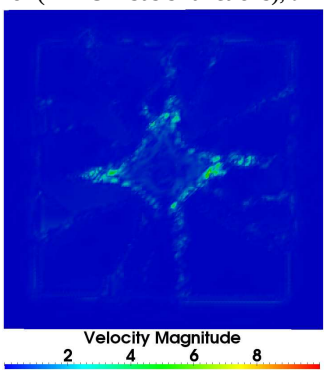

(e) error (50 POD basis functions), $t = 0.04\,s$

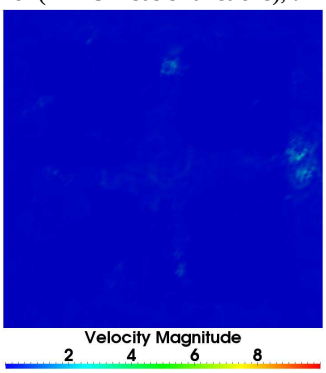

(f) error (50 POD basis functions), $t = 0.16\,s$

Figure 20: Case 2b: the difference of velocity solutions between the high fidelity model and NIROM using 6, 12 and 50 POD basis functions at time instances $t = 0.04\,s$ and $t = 0.16\,s$. The mean is not subtracted from the snapshots before constructing the POD basis functions.

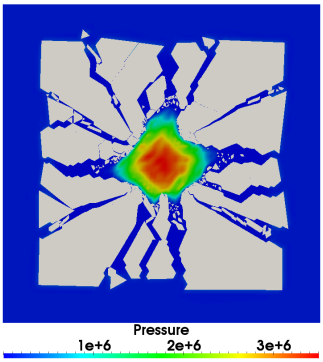

(a) high fidelity model, $t = 0.04\ s$

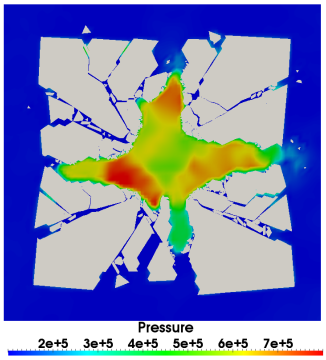

(b) high fidelity model, $t = 0.16\ s$

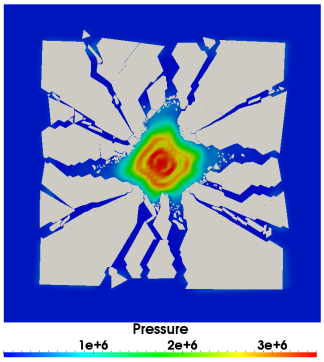

(c) NIROM (6 POD basis functions), $t = 0.04\ s$

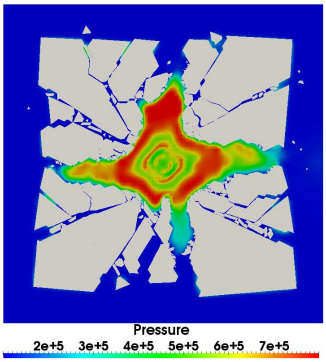

(d) NIROM (6 POD basis functions), $t = 0.16\ s$

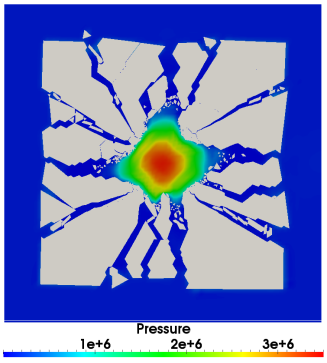

(e) NIROM (12 POD basis functions), $t = 0.04\ s$

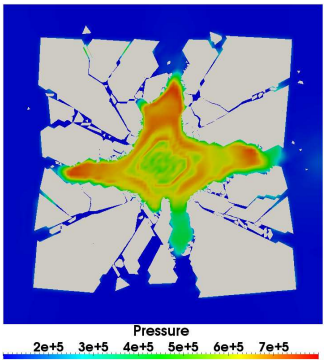

(f) NIROM (12 POD basis functions), $t = 0.16\ s$

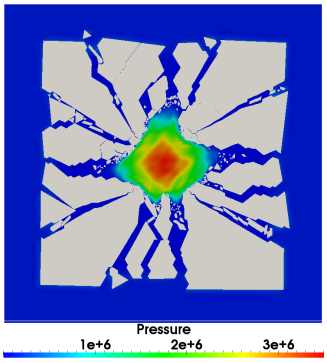

(g) NIROM (50 POD basis functions), $t = 0.04\ s$

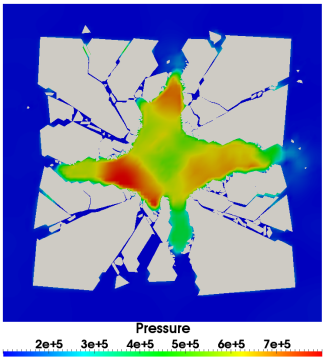

(h) NIROM (50 POD basis functions), $t = 0.16\ s$

Figure 21: Case 2b: comparison of pressure solutions between the high-fidelity model and NIROM with 6, 12 and 50 POD basis functions at time instances $t = 0.04\ s$ and $t = 0.16\ s$. The mean is not subtracted from the snapshots before constructing the POD basis functions.

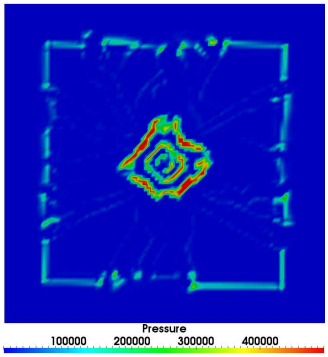

(a) error (6 POD basis functions), $t = 0.04$

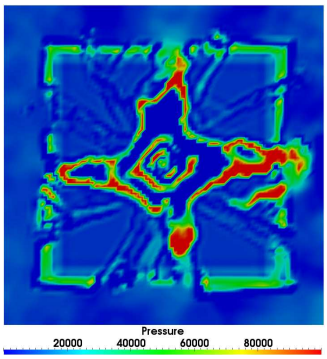

(b) error (6 POD basis functions), $t = 0.16$

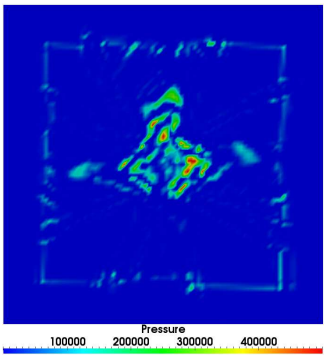

(c) error (12 POD basis functions), $t = 0.04\ s$

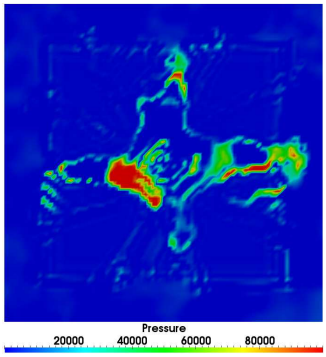

(d) error (12 POD basis functions), $t = 0.16\ s$

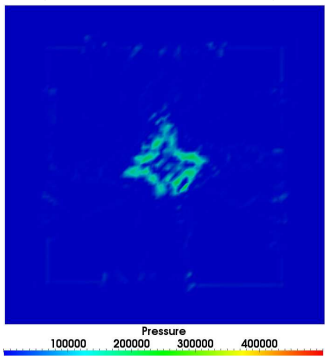

(e) error (50 POD basis functions), $t = 0.04\ s$

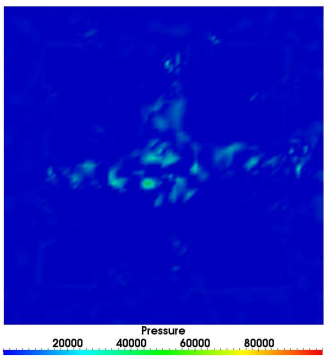

(f) error (50 POD basis functions), $t = 0.16\ s$

Figure 22: Case 2b: the difference of pressure solutions between the high fidelity model and NIROM with 6, 12 and 50 POD basis functions at time instances $t = 0.04\ s$ and $t = 0.16\ s$. The mean is not subtracted from the snapshots before constructing the POD basis functions.

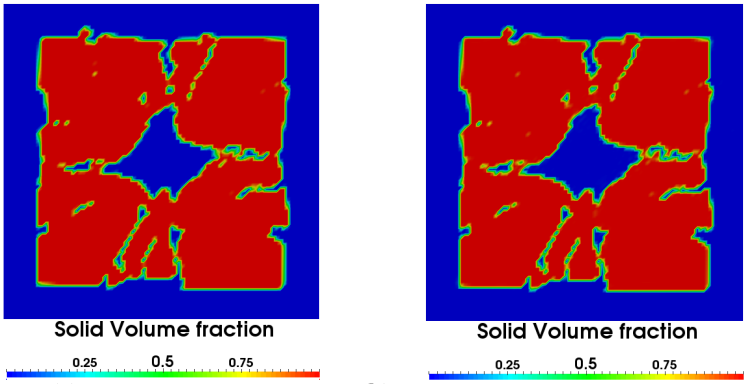

(a) Full model, $t = 0.04$ (b) NIROM (50 POD basis functions), $t = 0.04$

Figure 23: Case 2b: solid volume fraction solutions comparison between the high fidelity model and NIROM with 50 POD basis functions at time instances $t = 0.04\,s$. The mean is not subtracted from the snapshots before constructing the POD basis functions.

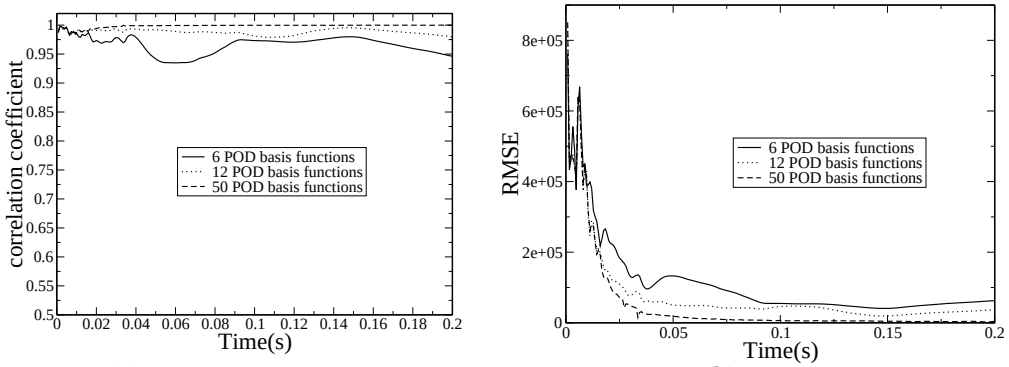

(a) Correlation coefficient (b) RMSE

Figure 24: Case 2b: the correlation coefficient and RMSE of pressure solutions between the high fidelity and NIROM with 6, 12 and 50 POD basis functions. The mean is not subtracted from the snapshots before constructing the POD basis functions.

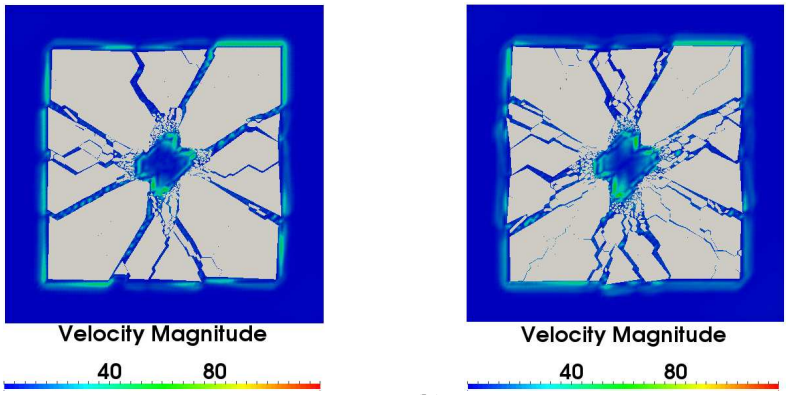

(a) full model with initial pressure of 387.45 (b) full model with initial pressure of 464.95

Figure 25: Case 2c: velocity solution from the high-fidelity full model with initial pressure of 387.45 and 464.95 at time level $t = 0.12\,s$

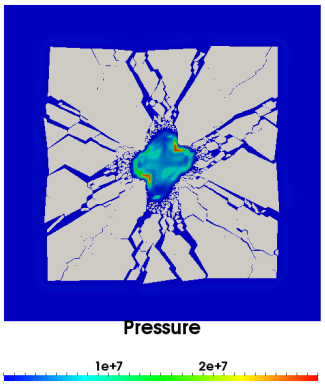

(a) full model pressure

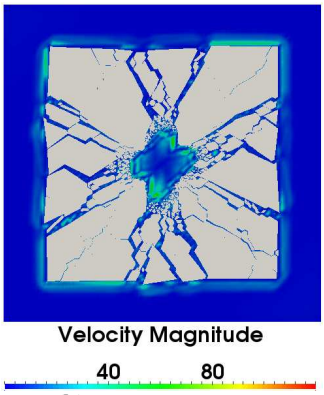

(b) full model velocity

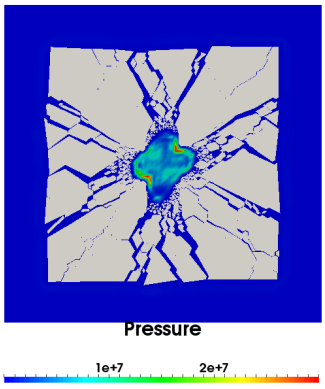

(c) NIROM (24 POD basis functions) pressure

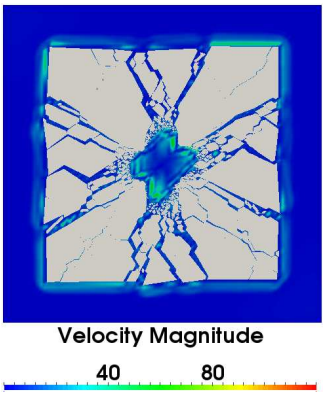

(d) NIROM (24 POD basis functions) velocity

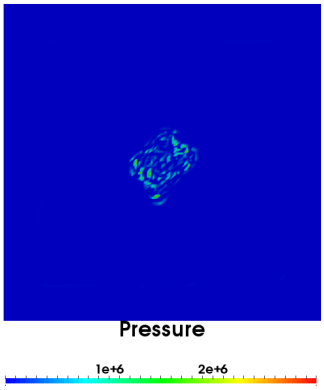

(e) NIROM pressure error distribution

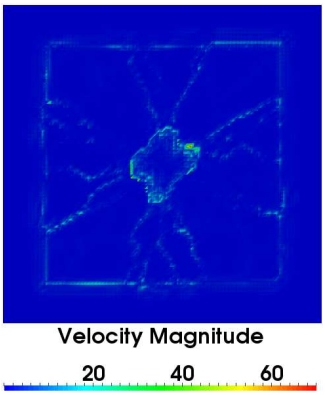

(f) NIROM velocity error distribution

Figure 26: Case 2c: pressure, velocity solutions of unseen initial pressure condition (464.95) obtained from the high-fidelity full model and NIROM with 24 POD basis functions at time level $t = 0.12\ s$

4.3. Efficiency of the NIROM

In this section, the online and offline computational costs are given. The offline cost can be defined as the time for precomputing while the online cost involves the simulation time when running the NIROM. The online computational time required for running the NIROM and high fidelity model are compared in Table 2, which includes the time required for the computational process in Algorithm 4. The simulations were carried out on a 12 cores (Intel(R) Xeon(R) X5680) workstation with 48GB RAM. During the simulations, only one core with 3.3GHz was used. The CPU time for constructing a set of hypersurfaces (see Algorithm 3) is offline, therefore, it is not listed in the table. As shown in Table 2, the computational time required for running the NIROM is decreased drastically in comparison with the high fidelity model. For example, in blasting test case with 48600 nodes, the CPU time for NIROM is reduced by 5 orders of magnitude.

Table 2: Comparison of the online CPU cost (seconds) required for running the high fidelity model and NIROM during one time level.

Cases	Model	Assembling and Solving	Projection	Interpolation	Total
an immersed wall	Full model	4.95120	0	0	4.95120
	NIROM	0	0.0003	0.0001	0.00040
Blasting	Full model	224.47059	0	0	224.47059
	NIROM	0	0.0003	0.0001	0.00040

The offline computational cost required for forming the NIROM includes the time for forming the POD basis functions and the hypersurfaces of the system dynamics. The time required for forming the hypersurfaces is very little and can be ignored. The CPU cost required for forming the POD basis functions is related to the number of POD basis functions, nodes and snapshots. The offline CPU cost required for forming the basis functions is listed in Table 3 where different numbers of POD basis functions are chosen and Table 4 using different number of snapshots. As shown in the tables the relationship between the offline CPU cost and the number of POD basis functions, nodes and snapshots is linear.

Table 3: Offline computational cost (seconds) required for constructing POD basis functions using different numbers of POD basis functions

Number of POD basis functions	12	18	30	nodes	snapshots
An immersed wall	17.93	18.11	18.53	7500	200
Number of POD basis functions	6	12	50	nodes	snapshots
Blasting	146.85	150.65	166.66	48600	200

5. Conclusions

A POD-RBF NIROM has been applied, for the first time, to a compressible fluid and fractured solid problem and implemented under the framework of a combined

Table 4: Offline computational cost (seconds) required for constructing POD basis functions using different numbers of snapshots

Number of snapshots	50	100	200	nodes	number of POD basis functions
An immersed wall	1.25	4.41	17.93	7500	12
Blasting	9.39	38.40	150.65	48600	12

finite-discrete element method based solid model (Y2D) and an unstructured mesh finite element model (Fluidity). The NIROM is independent of the governing equations and the source code, therefore, it is easy to modify. The performance of the NIROM for compressible fluid and fractured solid problems is numerically illustrated in two test cases: an immersed wall in a fluid and a blasting problem. The issue of whether or not the mean of solution snapshots should be subtracted before constructing the POD basis functions is addressed by comparing the NIROM results with those from the high fidelity model. An error analysis has been also carried out to validate and assess the performance of these different NIROM methods. It is found that the NIROM can perform much better when the mean is not subtracted from the snapshots before constructing the POD basis functions. The numerical results show that the best performing NIROM performs well and exhibits good agreement with the high fidelity model. We also demonstrated that NIROM is able to predict some problems that it has not seen before. The online CPU cost required for the NIROM is reduced by a factor of several orders of magnitude compared with the high fidelity full model. Future work includes extending this model to parametric problems with variable material properties.

Acknowledgments

This work was carried out under funding from Janet Watson scholarship at Department of Earth Science and Engineering. Authors would like to acknowledge the support of the UK's Natural Environment Research Council projects (NER/A/S/2003/00595, NE/C52101X/1 and NE/C51829X/1), the Engineering and Physical Sciences Research Council (GR/R60898, EP/I00405X/1 and EP/J002011/1), and the Imperial College High Performance Computing Service. Prof. I.M. Navon acknowledges the support of NSF/CMG grant ATM-0931198. Dr. Xiao acknowledges the support of NSFC grant 11502241. Dr. Chen and Dr. Xiang acknowledge the support of NSFC grant 51479146. Mr. Yang is grateful for the support of the China Scholarship Council (201406290056). Prof. Pain and Dr. Fang are grateful for the support provided by BP Exploration. Prof. Pain is grateful for the support of the EPSRC MEMPHIS multi-phase flow programme grant (EP/K003976/1). The authors acknowledge C. E. Haney for her comments that helped improve the manuscript. The authors acknowledge the support of EPSRC grant: Managing Air for Green Inner Cities (MAGIC)(EP/N010221/1).

References

[1] F. Fang, T. Zhang, D. Pavlidis, C. Pain, A. Buchan, and I. Navon, "Reduced order modelling of an unstructured mesh air pollution model and application in 2D/3D urban street canyons," *Atmospheric Environment*, vol. 96, pp. 96–106, 2014.

[2] F.Fang, C.Pain, I. Navon, A. Elsheikh, J. Du, and D.Xiao, "Non-linear Petrov-Galerkin methods for Reduced Order Hyperbolic Equations and Discontinuous Finite Element Methods," *Journal of Computational Physics*, vol. 234, pp. 540–559, 2013.

[3] R. Stefanescu and I. Navon, "POD/DEIM nonlinear model order reduction of an adi implicit shallow water equations model," *Journal of Computational Physics*, vol. 237, pp. 95–114, 2013.

[4] R. Stefanescu, A. Sandu, and I. Navon, "Comparison of POD reduced order strategies for the nonlinear 2D shallow water equations," *International Journal for Numerical Methods in Fluids*, vol. 76, no. 8, pp. 497–521, 2014.

[5] D. Daescu and I. Navon, "A dual-weighted approach to order reduction in 4D-Var data assimilation," *Monthly Weather Review*, vol. 136, no. 3, pp. 1026–1041, 2008.

[6] A. Manzoni, F. Salmoiraghi, and L. Heltai, "Reduced basis isogeometric methods (rb-iga) for the real-time simulation of potential flows about parametrized naca airfoils," *Computer Methods in Applied Mechanics and Engineering*, vol. 284, pp. 1147–1180, 2015.

[7] A. Buchan, A. Calloo, M. Goffin, S. Dargaville, F. Fang, C. Pain, and I. Navon, "A pod reduced order model for resolving angular direction in neutron/photon transport problems," *Journal of Computational Physics*, vol. 296, pp. 138–157, 2015.

[8] M. Alotaibi, V. M. Calo, Y. Efendiev, J. Galvis, and M. Ghommem, "Global–local nonlinear model reduction for flows in heterogeneous porous media," *Computer Methods in Applied Mechanics and Engineering*, vol. 292, pp. 122–137, 2015.

[9] M. Diez, E. F. Campana, and F. Stern, "Design-space dimensionality reduction in shape optimization by karhunen–loève expansion," *Computer Methods in Applied Mechanics and Engineering*, vol. 283, pp. 1525–1544, 2015.

[10] R. Abgrall, D. Amsallem, and R. Crisovan, "Robust model reduction by l^{1}-norm minimization and approximation via dictionaries: application to nonlinear hyperbolic problems," *Advanced Modeling and Simulation in Engineering Sciences*, vol. 3, no. 1, pp. 1–16, 2016.

[11] M. Schlegel and B. R. Noack, "On long-term boundedness of galerkin models," *Journal of Fluid Mechanics*, vol. 765, pp. 325–352, 2 2015.

[12] J. sth, B. R. Noack, S. Krajnovi, D. Barros, and J. Bore, "On the need for a nonlinear subscale turbulence term in pod models as exemplified for a high-reynolds-number flow over an ahmed body," *Journal of Fluid Mechanics*, vol. 747, pp. 518–544, 5 2014.

[13] L. P. Franca and S. L. Frey, "Stabilized finite element methods: Ii. the incompressible Navier-Stokes equations," *Computer Methods in Applied Mechanics and Engineering*, vol. 99, no. 2-3, pp. 209–233, 1992.

[14] S. Chaturantabut and D. Sorensen, "Nonlinear model reduction via discrete empirical interpolation," *SIAM J. Sci. Comput*, vol. 32, pp. 2737–2764, 2010.

[15] C. B.-M. K. Carlberg and C. Farhat, "Efficient non-linear model reduction via a least-squares Petrov-Galerkin projection and compressive tensor approximations," *International Journal for Numerical Methods in Engineering*, vol. 86, pp. 155–181, 2011.

[16] M. S. Y. Chu and J. Hahn, "State-preserving nonlinear model reduction procedure," *Chemical Engineering Science*, vol. 66, pp. 3907–3913, 2011.

[17] K. Willcox and A. Megretski, "Model reduction for large-scale linear applications," in *Proc. of 13th IFAC Symposium on System Identification, Rotterdam, Netherlands*, pp. 1431–1436, 2003.

[18] A. J. Feriedoun Sabetghadam, "α Regularization of the POD-Galerkin dynamical systems of the Kuramoto-Sivashinsky equation," *Applied Mathematics and Computation*, vol. 218, pp. 6012–6026, 2012.

[19] D. Xiao, F. Fang, J. Du, C. Pain, I. Navon, A. G. Buchan, A. ElSheikh, and G. Hu, "Non-linear Petrov-Galerkin methods for reduced order modelling of the Navier-Stokes equations using a mixed finite element pair," *Computer Methods In Applied Mechanics and Engineering*, vol. 255, pp. 147–157, 2013.

[20] M. Barrault, Y. Maday, N. Nguyen, and A. Patera, "An empirical interpolation method: application to efficient reduced-basis discretization of partial differential equations," *C. R. Acad. Sci. Paris, Ser*, vol. 339, pp. 667–672, 2004.

[21] J. Du, F. Fang, C. C. Pain, I. Navon, J. Zhu, and D. A. Ham, "POD reduced-order unstructured mesh modeling applied to 2d and 3d fluid flow," *Computers and Mathematics with Applications*, vol. 65, no. 3, pp. 362–379, 2013.

[22] F. Fang, C. Pain, I. Navon, M. Piggott, G. Gorman, P. Allison, and A. Goddard, "Reduced-order modelling of an adaptive mesh ocean model," *International journal for numerical methods in fluids*, vol. 59, no. 8, pp. 827–851, 2009.

[23] D. Xiao, F. Fang, A. G. Buchan, C. Pain, I. Navon*, D. J., , and G. Hu, "Non-linear model reduction for the Navier-Stokes equations using Residual DEIM method," *Journal of Computational Physics*, vol. 263, pp. 1–18, 2014.

[24] K. Carlberg, C. Farhat, J. Cortial, and D. Amsallem, "The GNAT method for nonlinear model reduction: effective implementation and application to computational fluid dynamics and turbulent flows," *Journal of Computational Physics*, vol. 242, pp. 623–647, 2013.

[25] M. F. Barone, I. Kalashnikova, M. R. Brake, and D. J. Segalman, "Reduced order modeling of fluid/structure interaction," *Sandia National Laboratories Report, SAND No*, vol. 7189, 2009.

[26] I. Kalashnikova, M. Barone, and M. Brake, "A stable Galerkin reduced order model for coupled fluid–structure interaction problems," *International Journal for Numerical Methods in Engineering*, vol. 95, no. 2, pp. 121–144, 2013.

[27] T. Lieu, C. Farhat, and M. Lesoinne, "Reduced-order fluid/structure modeling of a complete aircraft configuration," *Computer methods in applied mechanics and engineering*, vol. 195, no. 41, pp. 5730–5742, 2006.

[28] T. Lieu, C. Farhat, and M. Lesoinne, "Pod-based aeroelastic analysis of a complete f-16 configuration: Rom adaptation and demonstration," *AIAA Paper*, vol. 2295, p. 2005, 2005.

[29] E. Liberge, M. Pomarede, and A. Hamdouni, "Reduced-order modelling by pod-multiphase approach for fluid-structure interaction," *European Journal of Computational Mechanics/Revue Européenne de Mécanique Numérique*, vol. 19, no. 1-3, pp. 41–52, 2010.

[30] D. Forti and G. Rozza, "Efficient geometrical parametrisation techniques of interfaces for reduced-order modelling: application to fluid–structure interaction coupling problems," *International Journal of Computational Fluid Dynamics*, vol. 28, no. 3-4, pp. 158–169, 2014.

[31] M. Balajewicz, D. Amsallem, and C. Farhat, "Projection-based model reduction for contact problems," *International Journal for Numerical Methods in Engineering*, vol. 106, no. 8, pp. 644–663, 2016. nme.5135.

[32] C. Han, "Blackbox stencil interpolation method for model reduction," Master's thesis, Massachusetts Institute of Technology, 2012.

[33] S. Walton, O. Hassan, and K. Morgan, "Reduced order modelling for unsteady fluid flow using proper orthogonal decomposition and radial basis functions," *Applied Mathematical Modelling*, vol. 37, no. 20, pp. 8930–8945, 2013.

[34] D. Xiao, F. Fang, A. Buchan, C. Pain, I. Navon, and A. Muggeridge, "Non-intrusive reduced order modelling of the Navier–Stokes equations," *Computer Methods in Applied Mechanics and Engineering*, vol. 293, pp. 552–541, 2015.

[35] C. Audouze, F. De Vuyst, and P. B. Nair, "Nonintrusive reduced-order modeling of parametrized time-dependent partial differential equations," *Numerical Methods for Partial Differential Equations*, vol. 29, no. 5, pp. 1587–1628, 2013.

[36] C. Audouze, F. De Vuyst, and P. Nair, "Reduced-order modeling of parameterized PDEs using time–space-parameter principal component analysis," *International Journal for Numerical Methods in Engineering*, vol. 80, no. 8, pp. 1025–1057, 2009.

[37] D. Xiao, F. Fang, C. Pain, and G. Hu, "Non-intrusive reduced order modelling of the Navier-Stokes equations based on RBF interpolation," *International Journal for Numerical Methods in Fluids*, vol. 79, no. 11, pp. 580–595, 2015.

[38] D. Xiao, Z. Lin, F. Fang, C. Pain, I. Navon, P. Salinas, and A. Muggeridge, "Non-intrusive reduced order modeling for multiphase porous media flows using smolyak sparse grids," *International Journal for Numerical Methods in Fluids*, 2016.

[39] D. Xiao, P. Yang, F. Fang, J. Xiang, C. Pain, and I. Navon, "Non-intrusive reduced order modelling of fluidstructure interactions," *Computer Methods in Applied Mechanics and Engineering*, vol. 303, pp. 35 – 54, 2016.

[40] F. Ballarin and G. Rozza, "POD–Galerkin monolithic reduced order models for parametrized fluid-structure interaction problems," *International Journal for Numerical Methods in Fluids*, 2016.

[41] H. Chen, D. L. Reuss, and V. Sick, "On the use and interpretation of proper orthogonal decomposition of in-cylinder engine flows," *Measurement Science and Technology*, vol. 23, no. 8, p. 085302, 2012.

[42] M. Müller, *On the POD method: an abstract investigation with applications to reduced-order modeling and suboptimal control*. PhD thesis, Georg-August-Universitt zu Gttingen, 2008.

[43] H. Wang, J. Chessa, W. K. Liu, and T. Belytschko, "The immersed/fictitious element method for fluid–structure interaction: volumetric consistency, compressibility and thin members," *International Journal for Numerical Methods in Engineering*, vol. 74, no. 1, pp. 32–55, 2008.

[44] P. Yang, J. Xiang, M. Chen, F. Fang, D. Pavlidis, J. Latham, and C. Pain, "The immersed-body gas-solid interaction model for blast analysis in fractured solid media," *revision, International Journal of Rock Mechanics and Mining Sciences*, 2016.

[45] C. Pain, M. Piggott, A. Goddard, F. Fang, G. Gorman, D. Marshall, M. Eaton, P. Power, and C. De Oliveira, "Three-dimensional unstructured mesh ocean modelling," *Ocean Modelling*, vol. 10, no. 1, pp. 5–33, 2005.

[46] A. Munjiza, *The combined finite-discrete element method*. John Wiley & Sons, Ltd, 2004.

[47] AMCG and I. C. London, "Fluidity manual v4.1.12. figshare," *https://dx.doi.org/10.6084/m9.figshare.1387713.v2*, pp. 1–329, 2015.

[48] J. D. Anderson and J. Wendt, *Computational fluid dynamics*, vol. 206. Springer, 1995.

[49] L. Guo, J.-P. Latham, and J. Xiang, "Numerical simulation of breakages of concrete armour units using a three-dimensional fracture model in the context of the combined finite-discrete element method," *Computers & Structures*, vol. 146, pp. 117–142, 2015.

[50] A. Viré, J. Xiang, and C. Pain, "An immersed-shell method for modelling fluid–structure interactions," *Philosophical Transactions of the Royal Society of London A: Mathematical, Physical and Engineering Sciences*, vol. 373, no. 2035, p. 20140085, 2015.

[51] P. Yang, J. Xiang, F. Fang, D. Pavlidis, J.-P. Latham, and C. Pain, "Modelling of fluid-structure interaction with multiphase viscous flows using an immersed-body method," *Journal of Computational Physics*, 2016.

[52] A. Munjiza, K. Andrews, and J. White, "Combined single and smeared crack model in combined finite-discrete element analysis," *International Journal for Numerical Methods in Engineering*, vol. 44, no. 1, pp. 41–57, 1999.

[53] R. Bourguet, M. Braza, and A. Dervieux, "Reduced-order modeling for unsteady transonic flows around an airfoil," *Physics of Fluids (1994-present)*, vol. 19, no. 11, p. 111701, 2007.

[54] B. I. Epureanuj and J. Heeg, "Reduced order models in unsteady aerodynamics," 1999.

[55] D. J. Dalle, M. L. Fotia, and J. F. Driscoll, "Reduced-order modeling of two-dimensional supersonic flows with applications to scramjet inlets," *Journal of Propulsion and Power*, vol. 26, no. 3, pp. 545–555, 2010.

[56] K. Carlberg, J. Cortial, D. Amsallem, M. Zahr, and C. Farhat, "The gnat nonlinear model reduction method and its application to fluid dynamics problems," in *6th AIAA Theoretical Fluid Mechanics Conference, Honolulu, Hawaii, June*, vol. 2730, pp. 2011–3112, 2011.

[57] D. J. Lucia, "Reduced order modeling for high speed flows with moving shocks," tech. rep., DTIC Document, 2001.

[58] C. D. Marley, K. Duraisamy, and J. F. Driscoll, "Reduced order modeling of compressible flows with unsteady normal shock motion," in *51st AIAA/SAE/ASEE Joint Propulsion Conference*, p. 3988, 2015.

[59] T. R. White, "A clustering algorithm for reduced order modeling of shock waves," *technical report, Department of Mechanical Engineering, Stanford University*, 2015.